

CERN-PH-EP-2015-252
14 September 2015

Transverse momentum dependence of D-meson production in Pb–Pb collisions at $\sqrt{s_{NN}} = 2.76$ TeV

ALICE Collaboration*

Abstract

The production of prompt charmed mesons D^0 , D^+ and D^{*+} , and their antiparticles, was measured with the ALICE detector in Pb–Pb collisions at the centre-of-mass energy per nucleon pair, $\sqrt{s_{NN}}$, of 2.76 TeV. The production yields for rapidity $|y| < 0.5$ are presented as a function of transverse momentum, p_T , in the interval 1–36 GeV/ c for the centrality class 0–10% and in the interval 1–16 GeV/ c for the centrality class 30–50%. The nuclear modification factor R_{AA} was computed using a proton–proton reference at $\sqrt{s} = 2.76$ TeV, based on measurements at $\sqrt{s} = 7$ TeV and on theoretical calculations. A maximum suppression by a factor of 5–6 with respect to binary-scaled pp yields is observed for the most central collisions at p_T of about 10 GeV/ c . A suppression by a factor of about 2–3 persists at the highest p_T covered by the measurements. At low p_T (1–3 GeV/ c), the R_{AA} has large uncertainties that span the range 0.35 (factor of about 3 suppression) to 1 (no suppression). In all p_T intervals, the R_{AA} is larger in the 30–50% centrality class compared to central collisions. The D-meson R_{AA} is also compared with that of charged pions and, at large p_T , charged hadrons, and with model calculations.

arXiv:1509.06888v2 [nucl-ex] 9 Apr 2016

© 2015 CERN for the benefit of the ALICE Collaboration.

Reproduction of this article or parts of it is allowed as specified in the CC-BY-4.0 license.

*See Appendix A for the list of collaboration members

1 Introduction

A state of strongly-interacting matter characterised by high energy density and temperature is predicted to be formed in ultra-relativistic collisions of heavy nuclei. According to calculations using Quantum Chromodynamics (QCD) on the lattice, these extreme conditions lead to the formation of a Quark–Gluon Plasma (QGP) state, in which quarks and gluons are deconfined, and chiral symmetry is partially restored (see e.g. [1–4]).

Heavy quarks are produced in the hard scattering processes that occur in the early stage of the collision between partons of the incoming nuclei. Their production is characterised by a timescale $\Delta t < 1/(2m_{c,b})$, ~ 0.1 fm/ c for charm and ~ 0.01 fm/ c for beauty quarks, that is shorter than the formation time of the QGP medium, about 0.3 fm/ c at Large Hadron Collider (LHC) energies [5]. They can successively interact with the constituents of the medium and lose part of their energy, via inelastic processes (gluon radiation) [6, 7] or elastic scatterings (collisional processes) [8–10]. Energy loss can be studied using the nuclear modification factor R_{AA} , which compares the transverse-momentum (p_T) differential production yields in nucleus–nucleus collisions (dN_{AA}/dp_T) with the cross section in proton–proton collisions ($d\sigma_{pp}/dp_T$) scaled by the average nuclear overlap function ($\langle T_{AA} \rangle$)

$$R_{AA}(p_T) = \frac{1}{\langle T_{AA} \rangle} \cdot \frac{dN_{AA}/dp_T}{d\sigma_{pp}/dp_T}. \quad (1)$$

The average nuclear overlap function $\langle T_{AA} \rangle$ over a centrality class is proportional to the number of binary nucleon–nucleon collisions per A–A collision in that class and it can be estimated via Glauber model calculations [11, 12].

According to QCD calculations, quarks are expected to lose less energy than gluons because their coupling to the medium is smaller [6, 7]. In the energy regime of the LHC, light-flavour hadrons with p_T ranging from 5 to 20 GeV/ c originate predominantly from gluons produced in hard scattering processes, while for larger p_T they originate mainly from light quarks (see e.g. [13]). Charmed mesons, instead, provide an experimental tag for a quark parent at all momenta. Therefore, the comparison of the heavy-flavour hadron R_{AA} with that of pions is expected to be sensitive to the colour-charge dependence of energy loss. However, other aspects than the energy loss, like the parton p_T spectrum and fragmentation into hadrons, influence the nuclear modification factor (see e.g. [13, 14]). The effect of the colour-charge dependence of the energy loss should be then studied via the comparison with model calculations, that include the description of the aforementioned aspects.

In addition, several mass-dependent effects are predicted to influence the energy loss for quarks (see [15] for a recent review). The dead-cone effect should reduce small-angle gluon radiation for quarks that have moderate energy-over-mass values, i.e. for c and b quarks with momenta up to about 10 and 30 GeV/ c , respectively [16–22]. Likewise, collisional energy loss is predicted to be reduced for heavier quarks, because the spatial diffusion coefficient, which regulates the momentum transfers with the medium, scales with the inverse of the quark mass for a given quark momentum [23]. In particular, the study of D mesons from low- p_T to high- p_T allows to study the variation of the energy loss for different charm quark velocity: from a non-relativistic regime to an highly relativistic one. Low-momentum heavy quarks, including those shifted to low momentum by parton energy loss, could participate in the collective expansion of the system as a consequence of multiple interactions [24, 25]. It was also suggested that low-momentum heavy quarks could hadronise not only via fragmentation in the vacuum, but also via the mechanism of recombination with other quarks from the medium [25, 26].

The nuclear modification factor of heavy-flavour production was first studied at the Relativistic Heavy Ion Collider (RHIC). The PHENIX and STAR Collaborations reported measurements using heavy-flavour decay electrons and muons in Au–Au and Cu–Cu collisions at centre-of-mass energy per nucleon pair, $\sqrt{s_{NN}} = 200$ GeV [27–30]. A suppression with respect to binary scaling was observed for p_T

larger than about 3 GeV/ c , reaching a minimum R_{AA} of about 0.2–0.3 in the interval $4 < p_T < 6$ GeV/ c . The STAR Collaboration recently measured the R_{AA} of D^0 mesons in Au–Au collisions for the interval $0 < p_T < 6$ GeV/ c [31]. At p_T of about 5–6 GeV/ c the R_{AA} value is similar to that observed for electrons from heavy-flavour decays and the R_{AA} increases towards low p_T , reaching a maximum value of about 1.5 at 1–2 GeV/ c . This feature is described by heavy-flavour transport calculations that include radial flow and a contribution due to recombination in the charm hadronisation process [31].

A first measurement of the production of prompt D mesons at mid-rapidity in the p_T interval 2–16 GeV/ c was published, using the Pb–Pb data at $\sqrt{s_{NN}} = 2.76$ TeV collected in 2010 during LHC Run 1 [32]. A minimum R_{AA} of about 0.2–0.3 was measured at p_T of about 10 GeV/ c for the 20% most central collisions. The measurement of D-meson production in p–Pb collisions at $\sqrt{s_{NN}} = 5.02$ TeV, showing an R_{pPb} compatible with unity, has provided clear evidence that the suppression with respect to binary-scaled pp cross sections, observed in Pb–Pb collisions, cannot be attributed to cold nuclear matter effects for p_T larger than 2 GeV/ c and is, thus, caused by final-state interactions in the hot and dense medium [33].

In Pb–Pb collisions, the nuclear modification factor at low p_T results from the interplay of different effects occurring in the initial and in the final state. The measured D-meson nuclear modification factor in p–Pb collisions, although consistent with unity, is also described within uncertainties by calculations that include substantial initial-state effects, such as parton shadowing or saturation [33], that could manifest as a reduction of the yields in Pb–Pb (and thus of the R_{AA}) by up to 50% at low p_T . In addition, the measurement of a significant azimuthal anisotropy of D-meson production, with respect to the estimated direction of the reaction plane in non-central Pb–Pb collisions, indicates that charm quarks participate in the collective expansion of the medium [34, 35]. Therefore, radial flow could play a relevant role as well. In order to investigate these aspects, it is important to have a precise measurement of R_{AA} down to low p_T . In the high- p_T region, where parton energy loss is expected to be dominated by radiative processes, the extension of the D-meson R_{AA} beyond 20 GeV/ c would provide the first measurement of identified-hadron R_{AA} at such high p_T .

In this article we present the measurement of p_T -differential yields and nuclear modification factors of prompt D^0 , D^+ and D^{*+} mesons (including their antiparticles), reconstructed via their hadronic decays in Pb–Pb collisions at $\sqrt{s_{NN}} = 2.76$ TeV, using the data sample recorded in 2011. For central collisions, the integrated luminosity is larger by a factor of about 10 than that used for the previously published results [32]. This allows us to extend the measurement of R_{AA} to lower and higher p_T (from 2–16 GeV/ c to 1–36 GeV/ c), to improve its precision, and to perform the study in a narrower class of the most central collisions (10% most central instead of 20% most central).

The article is organised as follows: the experimental apparatus is described in Section 2, together with the data sample. In Section 3, the D-meson decay reconstruction and all corrections applied to the yields are presented, along with the procedure used to obtain the pp reference at $\sqrt{s} = 2.76$ TeV. In Section 4 the systematic uncertainties are discussed. The results for the 0–10% (central) and 30–50% (semi-peripheral) centrality classes are presented in Section 5. In the same Section results obtained in Pb–Pb collisions are compared with the nuclear modification factor measured in p–Pb collisions at $\sqrt{s_{NN}} = 5.02$ TeV. A comparison with charged pions, charged particles (ch) and with theoretical model predictions is also reported. These comparisons are presented in terms of the ratio $R_{AA}^D/R_{AA}^{\pi, ch}$ as well. Conclusions are drawn in Section 6.

2 Experimental apparatus and data sample

The ALICE experimental apparatus [36] is composed of various detectors for particle reconstruction and identification at mid-rapidity ($|\eta| < 0.9$), a forward muon spectrometer ($-4 < \eta < -2.5$) and a set of forward-backward detectors for triggering and event characterization. The detector performance for measurements in pp, p–Pb and Pb–Pb collisions from the LHC Run 1 is presented in [37].

The main detector components used in this analysis are the V0 detector, the Inner Tracking System (ITS), the Time Projection Chamber (TPC) and the Time Of Flight (TOF) detector, which are located inside a large solenoidal magnet providing a uniform magnetic field of 0.5 T parallel to the LHC beam direction (z axis in the ALICE reference system) and the Zero Degree Calorimeter (ZDC), located at ± 114 m from the interaction point.

Pb–Pb collision data were recorded with a minimum-bias interaction trigger based on information from the V0 detector, which consists of two scintillator arrays covering the full azimuth in the pseudorapidity intervals $-3.7 < \eta < -1.7$ and $2.8 < \eta < 5.1$ [38]. The trigger logic required the coincidence of signals on both sides of the detector. An online selection based on the V0 signal amplitudes was used to enhance the sample of central and mid-central collisions through two separate trigger classes. The scintillator arrays have an intrinsic time resolution better than 0.5 ns, and their timing information was used together with that from the ZDCs for offline rejection of events produced by the interaction of the beams with residual gas in the vacuum pipe. Only events with a reconstructed interaction point (primary vertex) within ± 10 cm from the centre of the detector along the beam line were used in the analysis.

Collisions were divided into centrality classes, determined from the sum of the V0 signal amplitudes and defined in terms of percentiles of the total hadronic Pb–Pb cross section. In order to relate the centrality classes to the collision geometry, the distribution of the V0 summed amplitudes was fitted with a function based on the Glauber model [11, 12] combined with a two-component model for particle production [39]. The centrality classes used in the analysis are reported in Tab. 1, together with the average of the nuclear overlap function T_{AA} , the number of events in each class (N_{events}) and the integrated luminosity.

The charged-particle tracks used to reconstruct the decay of D mesons were measured in the TPC and ITS. The tracking algorithm, based on a Kalman filter [40], starts from three-dimensional space points in the TPC, a large cylindrical drift detector with both total length and diameter of about 5 m, covering the pseudorapidity range $|\eta| < 0.9$ with full azimuthal acceptance [41]. Tracks are reconstructed in the TPC with up to 159 space points and with a measurement of the specific ionisation energy loss dE/dx with a resolution of about 6%.

Hits in the ITS are associated to the prolongation of the TPC tracks, forming the global tracks. The ITS consists of six cylindrical layers of silicon detectors [42]. The two innermost layers, placed at 3.9 and 7.6 cm from the beam line, consist of Silicon Pixel Detectors (SPD). The third and fourth layers use Silicon Drift Detectors (SDD) and the two outermost layers contain double-sided Silicon Strip Detectors (SSD). The effective spatial resolutions, including the intrinsic detector resolutions and residual misalignments, are about 14, 40 and 25 μm , for SPD, SDD and SSD, respectively, along the most precise direction ($r\phi$) [42].

Global tracks are used to reconstruct the primary interaction vertex and the secondary vertices of D-meson decays. The transverse momentum resolution for global tracks ranges from about 1% at $p_T = 1$ GeV/ c to about 2% at 10 GeV/ c , both in pp and Pb–Pb collisions. The spatial precision of global tracks is quantified by the resolution on the impact parameter d_0 , which is the signed distance of closest approach between the track and the primary vertex in the xy -plane transverse to the beam direction. In Pb–Pb collisions, the d_0 resolution is better than 65 μm for tracks with a transverse momentum larger

Centrality class	$\langle T_{AA} \rangle$ (mb^{-1})	N_{events}	L_{int} (μb^{-1})
0–10%	23.44 ± 0.76	16.4×10^6	21.3 ± 0.7
30–50%	3.87 ± 0.18	9.0×10^6	5.8 ± 0.2

Table 1: Average of the nuclear overlap function, number of events and integrated luminosity for the two centrality classes used in the analysis. The uncertainty on the integrated luminosity stems from the uncertainty of the hadronic Pb–Pb cross section from the Glauber model [39].

than 1 GeV/ c and reaches 20 μm for $p_T > 20$ GeV/ c [37].

The TOF detector is an array of Multi-Gap Resistive Plate Chambers positioned at a distance of about 370 cm from the beam line and covering the full azimuth over the pseudorapidity interval $|\eta| < 0.9$. TOF particle identification is based on the difference between the particle arrival time at the TOF detector and a start time determined using the arrival time of all particles of the event with a χ^2 minimization [43]. The resolution (σ) of the time-of-flight measurement is about 80 ps for pions at $p_T = 1$ GeV/ c in the Pb–Pb collision centrality intervals used in this analysis. TOF provides charged-particle identification in the intermediate momentum range, with a 3σ separation up to about 2.5 GeV/ c for pions and kaons, and up to about 4 GeV/ c for kaons and protons [37].

3 Data analysis

3.1 D-meson reconstruction

D^0 , D^+ and D^{*+} mesons, and their antiparticles, were reconstructed via their hadronic decay channels $D^0 \rightarrow K^- \pi^+$ (weak decay with branching ratio, BR, of $3.88 \pm 0.05\%$), $D^+ \rightarrow K^- \pi^+ \pi^+$ (weak decay, BR of $9.13 \pm 0.19\%$) and $D^{*+} \rightarrow D^0 \pi^+$ (strong decay, BR of $67.7 \pm 0.05\%$) followed by $D^0 \rightarrow K^- \pi^+$ [44]. D^0 and D^+ mesons have mean proper decay lengths ($c\tau$) of 123 and 312 μm , respectively [44]. In the case of the D^{*+} , the decay topology of the produced D^0 was exploited. The transverse momentum of the soft pions produced in the D^{*+} decays typically ranges from 0.1 to 1.5 GeV/ c , depending on the D^{*+} p_T .

D^0 and D^+ candidates were formed using pairs and triplets of tracks with the correct charge-sign combination, requiring $|\eta| < 0.8$, $p_T > 0.4$ GeV/ c , at least 70 associated space points (out of a maximum of 159) and fit quality $\chi^2/\text{ndf} < 2$ in the TPC, and at least two hits (out of six) in the ITS, out of which at least one in either of the two SPD layers. D^{*+} candidates were formed by combining D^0 candidates with tracks with $p_T > 0.1$ GeV/ c and at least three hits in the ITS, out of which at least one in the SPD.

The aforementioned track selection limits the D-meson acceptance in rapidity. The acceptance drops steeply to zero for $|y| > 0.5$ at low p_T and $|y| > 0.8$ for $p_T > 5$ GeV/ c . A p_T -dependent fiducial acceptance cut, $|y_D| < y_{\text{fid}}(p_T)$, was therefore applied to the D-meson rapidity. The cut value, $y_{\text{fid}}(p_T)$, increases from 0.5 to 0.8 in the range $0 < p_T < 5$ GeV/ c according to a second-order polynomial function and with a constant value of 0.8 for $p_T > 5$ GeV/ c .

The selection of the decay topology was based on the displacement of the decay tracks from the interaction vertex (via their impact parameter, d_0), the separation between the secondary and primary vertices (decay length, L) and the pointing angle of the reconstructed D-meson momentum to the primary vertex. This pointing condition was applied via a selection on the angle θ_{pointing} between the direction of the reconstructed momentum of the candidate and the straight line connecting the primary and secondary vertices. The projections of the pointing angle and of the decay length onto the transverse plane ($\theta_{\text{pointing}}^{\text{xy}}$ and L^{xy}) were also used. The selection requirements were tuned to provide a large statistical significance for the signal and to keep the selection efficiency as high as possible. The chosen selection values depend on the p_T of the D meson and become tighter from peripheral to central collisions. A detailed description of the selection criteria was reported in [32, 35].

In order to further reduce the combinatorial background, pions and kaons were identified using the TPC and TOF detectors. A 3σ compatibility cut was applied to the difference between the measured and expected signals (for pions and kaons) for the TPC dE/dx and TOF time-of-flight. Tracks that are not matched with a hit in the TOF detector were identified using only the TPC information. Particle identification (PID) was not applied to the pion track from the D^{*+} decay. This PID selection provides a reduction of the background by a factor of 2–3 at low p_T with respect to the case without applying the selection, while having an efficiency of about 95% for the signal.

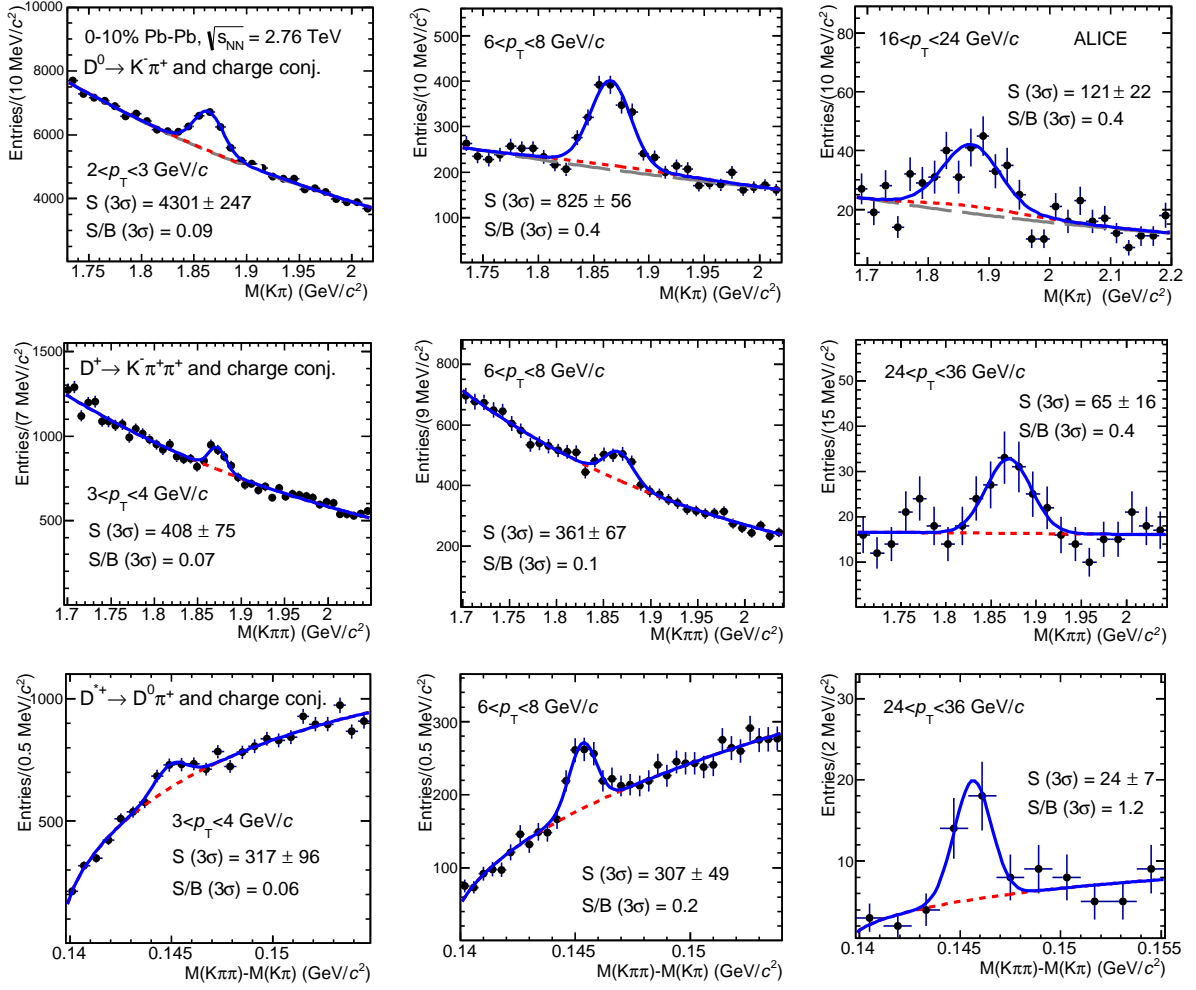


Figure 1: (K, π) (top row) and (K, π, π) (central row) invariant-mass distributions for the centrality class 0–10%. Bottom row: Distribution of the mass difference $\Delta M = M(K\pi\pi) - M(K\pi)$ for the centrality class 0–10%. The distributions are reported in three p_T intervals for each meson (left, middle and right column). The fit functions used to describe the background (dash), the background without signal reflections (only for D^0 , long-dash) and the total distribution including the signal (solid) are shown.

The raw D-meson yields were obtained from fits to the candidate invariant-mass distributions $M(K\pi)$ for D^0 , $M(K\pi\pi)$ for D^+ , and the mass difference $\Delta M = M(K\pi\pi) - M(K\pi)$ for D^{*+} . The D^0 and D^+ candidate invariant-mass distributions were fitted with a function composed of a Gaussian for the signal and an exponential term to describe the background shape. In the 0–10% centrality class, the background in the $M(K\pi)$ distribution for the interval $1 < p_T < 2$ GeV/c could not be accounted for by an exponential shape and was instead modelled with a fourth-order polynomial function. The ΔM distribution of D^{*+} candidates was fitted with a Gaussian function for the signal and a threshold function multiplied by an exponential for the background: $a\sqrt{\Delta M - m_\pi} \cdot e^{b(\Delta M - m_\pi)}$.

In the case of D^0 mesons, an additional term was included in the fit function to account for the background from “reflections”, i.e. signal candidates that remain in the invariant-mass distribution when the (K, π) mass hypotheses for the two decay tracks are swapped. A study of simulations showed that about 70% of these reflections are rejected by the PID selection, while the residual contribution results in a broad invariant-mass distribution, which can be described using a sum of two Gaussians. In order to account for the contribution of reflections in the data (2–5% at low p_T , about 10% at high p_T), a template consisting

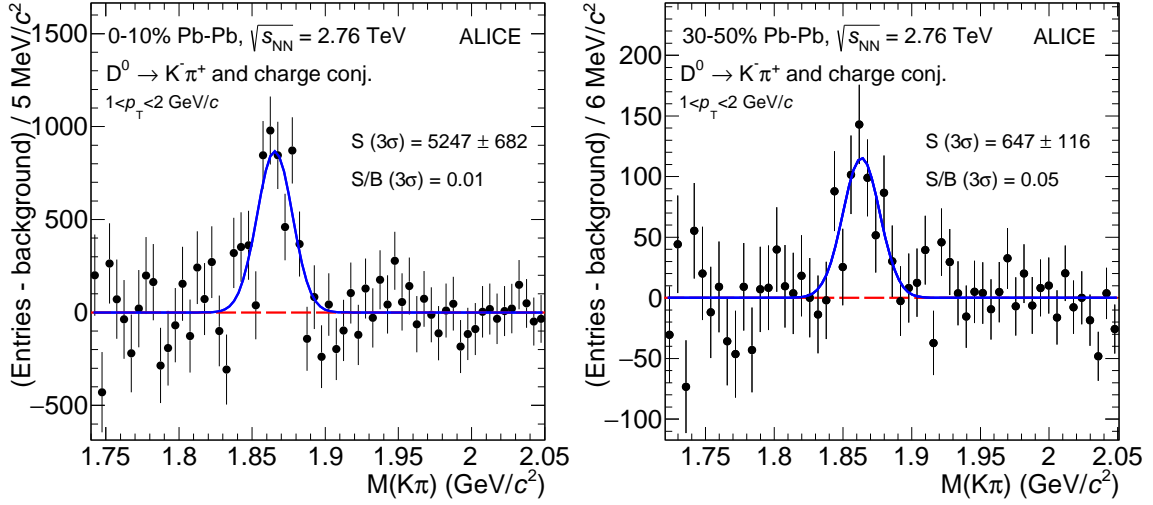


Figure 2: (K, π) invariant-mass distribution for the interval $1 < p_T < 2$ GeV/ c for the 0–10% (left) and 30–50% (right) centrality classes, obtained after the subtraction of the background estimated by a fourth-order polynomial function for the most central collisions and an exponential for the 30–50% centrality class. The contribution of reflections is also included in the fit. The fit function used to describe the signal (solid line) is shown.

of two Gaussians was included in the fit. The centroids and widths, as well as the ratios of the integrals of these Gaussians to the signal integral, were fixed to the values obtained in the simulations (see also [35]).

In the centrality class 0–10%, the signal extraction was performed in the interval $1 < p_T < 24$ GeV/ c for D^0 mesons, divided in 9 p_T bins, and in the interval $3 < p_T < 36$ GeV/ c for D^+ and D^{*+} mesons, divided in 8 p_T bins. In the centrality class 30–50%, the signal extraction was possible in the interval $1 < p_T < 16$ GeV/ c for D^0 mesons and in the interval $2 < p_T < 16$ GeV/ c for D^+ and D^{*+} mesons. Beyond these intervals, the signal extraction was prevented by the low signal-over-background ratio at low p_T , and by the low signal yield at high p_T . Figure 1 shows the D^0 and D^+ invariant-mass distributions and D^{*+} mass difference distributions in three p_T intervals for the centrality class 0–10%. In the interval $16 < p_T < 24$ GeV/ c the fit range for the D^0 case is asymmetric. The range was limited to values larger than 1.68 GeV/ c^2 because the invariant-mass distribution of (K, π) pairs from D mesons decaying in three or more prongs produces a wide structure below about 1.72 GeV/ c^2 , which cannot be accounted for by the background terms of the fit function.

Figure 2 shows the background-subtracted D^0 invariant-mass distribution for the interval $1 < p_T < 2$ GeV/ c for the 0–10% (left panel) and 30–50% (right panel) centrality classes.

For all three D-meson species, the position of the signal peak was found to be compatible with the world average value and its p_T -dependent width with the values observed in the simulation. The statistical significance of the observed signals $S/\sqrt{S+B}$ varies from 3 to 18, while the signal-over-background ratio S/B ranges from 0.01 to 1.8, depending on the meson species, p_T interval and centrality class.

3.2 dN/dp_T spectra corrections

The D-meson raw yields were corrected in order to obtain the p_T -differential yields of prompt D mesons

$$\left. \frac{dN^D}{dp_T} \right|_{|y| < 0.5} = \frac{f_{\text{prompt}}(p_T) \cdot \frac{1}{2} N_{\text{raw}}^{D+\bar{D}}(p_T) \Big|_{|y| < y_{\text{fid}}}}{\Delta p_T \cdot \alpha_y \cdot (\text{Acc} \times \epsilon)_{\text{prompt}}(p_T) \cdot \text{BR} \cdot N_{\text{events}}}, \quad (2)$$

where prompt refers to mesons not coming from weak decays of B hadrons. The raw yields $N_{\text{raw}}^{\text{D}+\bar{\text{D}}}$ were divided by a factor of two to obtain the charge-averaged (particle and antiparticle) yields. To correct for the contribution of B-meson decay feed-down, the raw yields were multiplied by the fraction of promptly produced D mesons, f_{prompt} (discussed in details later in this section). Furthermore, they were divided by the product of prompt D-meson acceptance and efficiency $(\text{Acc} \times \varepsilon)_{\text{prompt}}$, by the decay channel branching ratio (BR), by the transverse momentum interval width (Δp_{T}) and by the number of events (N_{events}). The factor $\alpha_y = y_{\text{fid}}/0.5$ normalises the corrected yields measured in $|y| < y_{\text{fid}}$ to one unit of rapidity $|y| < 0.5$, assuming a uniform rapidity distribution for D mesons in the measured range. This assumption was validated to the 1% level with simulations [45, 46].

The correction for acceptance and efficiency $(\text{Acc} \times \varepsilon)_{\text{prompt}}$ was determined using Monte Carlo simulations with a detailed description of the detector and its response, based on the GEANT3 transport package [47]. The simulation was tuned to reproduce the (time-dependent) position and width of the interaction vertex distribution, as well as the number of active read-out channels and the accuracy of the detector calibration. The underlying Pb–Pb events at $\sqrt{s_{\text{NN}}} = 2.76$ TeV were simulated using the HIJING v1.383 generator [48] and D-meson signals were added with the PYTHIA v6.421 generator [49] with Perugia-0 tune [50]. Each simulated PYTHIA pp event contained a $c\bar{c}$ or $b\bar{b}$ pair, and D mesons were forced to decay in the hadronic channels of interest for the analysis. Out of all the particles produced in these PYTHIA pp events, only the heavy-flavour decay products were kept and transported through the detector simulation together with the particles produced according to HIJING. In order to minimise the bias on the detector occupancy, the number of D mesons injected into each HIJING event was adjusted according to the Pb–Pb collision centrality. In the most central event class, the p_{T} distribution of D mesons was weighted in order to match the shape measured for the D^0 meson. In the semi-peripheral centrality class, the D-meson p_{T} distribution was weighted so as to match the shape given by fixed-order-next-to-leading-log perturbative QCD calculations (FONLL) [51, 52] multiplied by the $R_{\text{AA}}(p_{\text{T}})$ computed using the BAMPS model [53–55].

The efficiencies were evaluated from simulated events that have the same average charged-particle multiplicity, corresponding to the same detector occupancy, as observed in data in the centrality classes 0–10% and 30–50%. Figure 3 shows the D^0 , D^+ and D^{*+} acceptance-times-efficiency $(\text{Acc} \times \varepsilon)$ for primary and feed-down D mesons with rapidity $|y| < y_{\text{fid}}(p_{\text{T}})$ in the centrality class 0–10%. The efficiencies range from about 0.1% at low p_{T} to 10–30% at high p_{T} , because of the momentum dependence of the D-meson decay length and of the topological selections applied in the different momentum intervals. Also shown in the figure are the $(\text{Acc} \times \varepsilon)$ values for the case where no PID is applied. The relative difference with respect to the $(\text{Acc} \times \varepsilon)$ obtained using the PID selection is about 5%, illustrating the high efficiency of the PID criteria. The $(\text{Acc} \times \varepsilon)$ for D mesons from B-meson decays is larger than for prompt D mesons by a factor of about 1.5, because the decay vertices of the feed-down D mesons are more separated from the primary vertex and are, therefore, more efficiently selected by the analysis cuts.

The f_{prompt} factor was obtained, following the procedure introduced in [32], as

$$\begin{aligned} f_{\text{prompt}} &= 1 - \frac{N_{\text{raw}}^{\text{D}+\bar{\text{D}}\text{feed-down}}}{N_{\text{raw}}^{\text{D}+\bar{\text{D}}}} \\ &= 1 - R_{\text{AA}}^{\text{feed-down}} \cdot \langle T_{\text{AA}} \rangle \cdot \left(\frac{d\sigma}{dp_{\text{T}}} \right)_{\text{feed-down}, |y| < 0.5}^{\text{FONLL, EvtGen}} \cdot \frac{\Delta p_{\text{T}} \cdot \alpha_y \cdot (\text{Acc} \times \varepsilon)_{\text{feed-down}} \cdot \text{BR} \cdot N_{\text{events}}}{\frac{1}{2} N_{\text{raw}}^{\text{D}+\bar{\text{D}}}}. \end{aligned} \quad (3)$$

In this expression, the symbols denoting the p_{T} dependence have been omitted for brevity, $N_{\text{raw}}^{\text{D}+\bar{\text{D}}}$ is the measured raw yields and $N_{\text{raw}}^{\text{D}+\bar{\text{D}}\text{feed-down}}$ is the estimated raw yields of D mesons from B-meson decays. In detail, the B-meson production cross section in pp collisions at $\sqrt{s} = 2.76$ TeV, estimated with FONLL calculations [56], was folded with the $\text{B} \rightarrow \text{D} + \text{X}$ decay kinematics using the EvtGen package [57] and multiplied by $\langle T_{\text{AA}} \rangle$ in each centrality class, by the $(\text{Acc} \times \varepsilon)$ for feed-down D mesons, and by the other

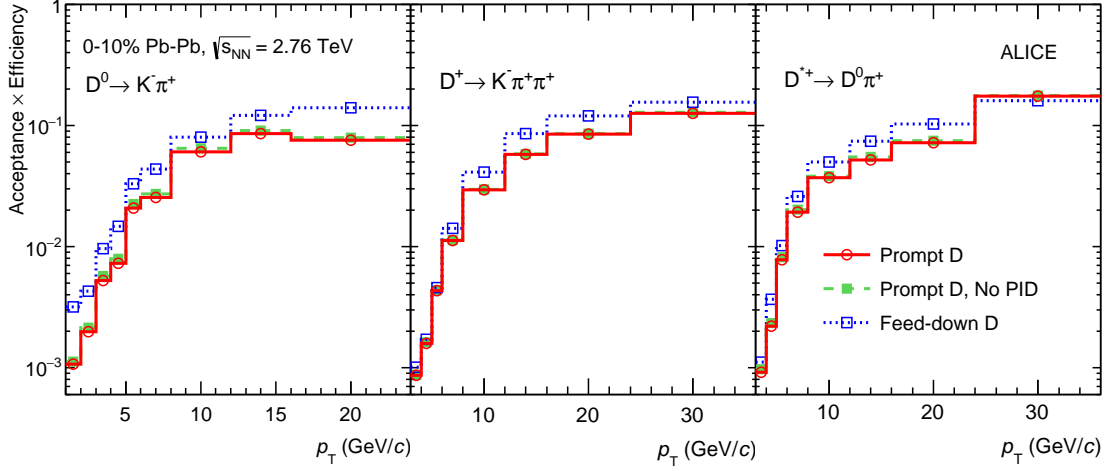


Figure 3: Product of acceptance and efficiency for D mesons in Pb–Pb collisions for the 0–10% centrality class. The rapidity interval is $|y| < y_{\text{fid}}$ (see Section 3.1). The values for prompt (solid lines) and feed-down (dotted lines) D mesons are shown. Also displayed, for comparison, are the values for prompt D mesons without PID selection (dashed lines).

factors introduced in Eq. (2). In addition, the nuclear modification factor of D mesons from B-meson decays was accounted for. The comparison of the R_{AA} of prompt D mesons (R_{AA}^{prompt}) [58] with that of J/ψ from B-meson decays [59] measured in the CMS experiment indicates that charmed hadrons are more suppressed than beauty hadrons. The value $R_{AA}^{\text{feed-down}} = 2 \cdot R_{AA}^{\text{prompt}}$ was used to compute the correction, and the variation over the range $1 < R_{AA}^{\text{feed-down}}/R_{AA}^{\text{prompt}} < 3$ was considered for the evaluation of the systematic uncertainties, in order to take into account possible centrality and p_T dependences. Assuming $R_{AA}^{\text{feed-down}} = 2 \cdot R_{AA}^{\text{prompt}}$, the resulting f_{prompt} ranges from about 0.65 to 0.85, depending on the D-meson species and on the p_T interval.

3.3 Proton–proton reference for R_{AA}

The p_T -differential cross section of prompt D mesons with $|y| < 0.5$ in pp collisions at $\sqrt{s} = 2.76$ TeV, used as reference for the nuclear modification factor, was obtained as follows:

- in the interval $2 < p_T < 16$ (24) GeV/c for D^0 (D^+ and D^{*+}), the measurement at $\sqrt{s} = 7$ TeV [45] scaled to $\sqrt{s} = 2.76$ TeV with FONLL calculations [56] was used;
- in the interval $1 < p_T < 2$ GeV/c for D^0 , an average of the aforementioned $\sqrt{s} = 7$ TeV scaled measurement and of the measurement at $\sqrt{s} = 2.76$ TeV [60] was used;
- in the interval 16 (24) $< p_T < 24$ (36) GeV/c for D^0 (D^+ and D^{*+}), where their cross sections were not measured in pp collisions, the FONLL calculation at $\sqrt{s} = 2.76$ TeV [56] was used as a reference, after scaling it to match the central value of the data at lower p_T .

The p_T -dependent scaling factor from $\sqrt{s} = 7$ TeV to $\sqrt{s} = 2.76$ TeV was determined with FONLL calculations and its uncertainties were determined by varying the parameters (charm-quark mass, factorisation and renormalisation scales) as described in [61]. The uncertainties on the scaling factor range from $^{+57}_{-11}\%$ for $1 < p_T < 2$ GeV/c to about $\pm 5\%$ for $p_T > 10$ GeV/c. The result of the scaling of the $\sqrt{s} = 7$ TeV p_T -differential cross sections to $\sqrt{s} = 2.76$ TeV was validated with measurements from a

smaller data sample in pp collisions at $\sqrt{s} = 2.76$ TeV [60]. These measurements cover a reduced p_T interval with a statistical uncertainty of 20–25% and therefore they were not used as a pp reference for $p_T > 2$ GeV/ c .

For the lowest p_T interval for the D^0 meson, the two references (obtained from the measurement in pp collisions at $\sqrt{s} = 2.76$ TeV and from the $\sqrt{s} = 7$ TeV scaled measurement) have comparable uncertainties. Therefore, in this interval, the two values were averaged using the inverse of the squared relative uncertainties as weights. In particular, the statistical uncertainties and the uncorrelated part of the systematic uncertainties, i.e. the systematic uncertainty from data analysis (yield extraction, efficiency corrections) and the scaling uncertainty, were used in the weight. The uncertainties on the feed-down subtraction were considered as fully correlated among the two measurements, and were propagated linearly.

The cross section measurements for D mesons in pp collisions at $\sqrt{s} = 7$ TeV are limited to $p_T \leq 16$ GeV/ c for D^0 and to $p_T \leq 24$ GeV/ c for D^+ and D^{*+} . Beyond these limits the pp reference was obtained using the cross section from the FONLL calculation at $\sqrt{s} = 2.76$ TeV [56]. Since the central value of the FONLL calculation underestimates the measurement for $p_T > 5$ GeV/ c at both $\sqrt{s} = 2.76$ TeV and $\sqrt{s} = 7$ TeV [45, 60], the FONLL cross section was multiplied by a scaling factor (κ)

$$\frac{d\sigma}{dp_T} = \kappa \cdot \left(\frac{d\sigma}{dp_T} \right)_{\sqrt{s}=2.76\text{TeV}, |y|<0.5}^{\text{FONLL}}. \quad (4)$$

The factor κ was determined by fitting with a constant the data-to-theory ratio at $\sqrt{s} = 7$ TeV in the interval $5 < p_T < 16$ GeV/ c . Since the measurements at $\sqrt{s} = 2.76$ TeV are less precise, they do not constrain further the scaling factor. Depending on the D-meson species, the factor κ ranges from 1.4 to 1.5, for the central values of the FONLL calculation parameters [56]. The statistical uncertainty of the extrapolated cross section was determined by propagating the statistical uncertainties of the measurement in the determination of κ and it amounts to about 5%. The systematic uncertainties were evaluated under the conservative assumption that the systematic uncertainties of the measurement are fully correlated over p_T , i.e. by repeating the calculation of κ after shifting all data points consistently within their systematic uncertainties. In addition, the calculation in Eq. (4) was performed considering the FONLL cross sections obtained from combinations of the renormalisation and factorisation scales with values $(0.5, 1, 2) \cdot \sqrt{m_c^2 + p_{T,c}^2}$ [56], as well as the upper and lower limits of their envelope¹. This resulted in a total systematic uncertainty on the p_T -extrapolated cross section of about ${}^{+50}_{-35}\%$.

4 Systematic uncertainties

4.1 Systematic uncertainties on the D-meson p_T spectra

The systematic uncertainties were estimated as a function of transverse momentum for the two centrality classes. Table 2 lists the uncertainties for three p_T intervals for each meson species.

The systematic uncertainty on the raw yield extraction was evaluated by repeating the fit of the invariant-mass distributions while varying the fit range; by fixing the mean and sigma of the Gaussian term to the world-average value and the expectations from Monte Carlo simulations, respectively; and by using different fit functions for the background. Specifically, first- and second-order polynomials were used for D^0 and D^+ , and a power law multiplied by an exponential or a threshold function for D^{*+} . A method based on bin counting of the signal after background subtraction was also used. This method does not assume any particular shape for the invariant-mass distribution of the signal. The estimated uncertainties depend on the centrality class and on the p_T interval, ranging from 5% to 15% for D^0 , 8% to 10% for D^+ and 5% to 10% for D^{*+} , typically with larger values in the lowest and highest p_T intervals.

¹Where m_c and $p_{T,c}$ are respectively the mass and the transverse momentum of the charm quark considered in the calculations.

Particle	D ⁰			D ⁺			D ^{*+}		
0–10% centrality class									
p_T interval (GeV/ c)	1–2	6–8	16–24	3–4	6–8	24–36	3–4	6–8	24–36
Yield extraction	15%	5%	15%	10%	8%	8%	12%	5%	10%
Tracking efficiency	10%	10%	10%	15%	15%	15%	15%	15%	15%
Selection cuts	15%	5%	5%	10%	10%	10%	10%	10%	10%
PID efficiency	5%	5%	5%	5%	5%	5%	5%	5%	5%
MC p_T shape	15%	1%	1%	6%	1%	1%	4%	1%	1%
FONLL feed-down corr.	+5% –45%	+8% –13%	+10% –16%	+4% –12%	+6% –11%	+8% –14%	+3% –12%	+4% –7%	+3% –8%
$R_{AA}^{\text{feed-down}}/R_{AA}^{\text{prompt}}$ (Eq. (3))	+5% –5%	+11% –10%	+16% –13%	+6% –5%	+9% –7%	+14% –11%	+4% –4%	+6% –6%	+6% –6%
BR		1.3%			2.1%			1.5%	
Centrality class definition		< 1%			< 1%			< 1%	
30–50% centrality class									
p_T interval (GeV/ c)	1–2	6–8	12–16	2–3	6–8	12–16	2–3	6–8	12–16
Yield extraction	10%	8%	8%	10%	10%	12%	12%	8%	5%
Tracking efficiency	10%	10%	10%	15%	15%	15%	15%	15%	15%
Selection cuts	10%	10%	15%	10%	10%	15%	15%	10%	5%
PID efficiency	5%	5%	5%	5%	5%	5%	5%	5%	5%
MC p_T shape	5%	1%	3%	10%	2%	2%	10%	1%	1%
FONLL feed-down corr.	+5% –45%	+7% –12%	+8% –11%	+6% –21%	+6% –12%	+11% –13%	+3% –19%	+5% –8%	+4% –8%
$R_{AA}^{\text{feed-down}}/R_{AA}^{\text{prompt}}$ (Eq. (3))	+6% –5%	+11% –9%	+14% –11%	+7% –6%	+9% –8%	+16% –12%	+4% –4%	+7% –6%	+6% –6%
BR		1.3%			2.1%			1.5%	
Centrality class definition		2%			2%			2%	

Table 2: Relative systematic uncertainties on the prompt D-meson production yields in Pb–Pb collisions for three selected p_T intervals, in the two centrality classes.

For D⁰ mesons, the systematic uncertainty due to signal reflections in the invariant-mass distribution was estimated by changing by $\pm 50\%$ the ratio of the integral of the reflections over the integral of the signal (obtained from the simulation) used in the invariant-mass fit with the reflections template. In addition, the shape of the template was varied using a polynomial parameterisation (of third or sixth order) of the simulated distribution, instead of a double-Gaussian parameterisation. A test was carried out using, in the fit, a template histogram of the reflections obtained directly from the simulation, rather than a functional form. The variation observed in the raw yields, ranging from 3% to 7% from low to high p_T , was added in quadrature as an independent contribution to the yield extraction systematic uncertainty.

The systematic uncertainty on the tracking efficiency was estimated by comparing the probability to match the TPC tracks to the ITS hits in data and simulation, and by varying the track quality selection criteria (for example, the minimum number of associated hits in the TPC and in the ITS, and the maximum χ^2/ndf of the momentum fit). The efficiency of the track matching and the association of hits in the silicon pixel layers was found to be well reproduced by the simulation with maximal deviations on the level of 5% in the p_T range relevant for this analysis (0.5–25 GeV/ c) [37]. The effect of mis-associating ITS hits to tracks was studied using simulations. The mis-association probability is about 5%, for central collisions, in the transverse momentum interval $1 < p_T < 3$ GeV/ c and drops rapidly to zero at larger p_T .

It was verified that the signal selection efficiencies are the same for D mesons with and without wrong hit associations. The total systematic uncertainty on the track reconstruction procedure amounts to 5% for single tracks, which results in a 10% uncertainty for D^0 mesons (two-tracks decay) and 15% for D^+ and D^{*+} mesons (three-tracks decay).

The uncertainty on the D-meson selection efficiency reflects a possible non-exact description of the D-meson kinematic properties and of the detector resolutions and alignments in the simulation. This effect was estimated by repeating the analysis with different values of the selection cuts, significantly modifying the efficiencies, raw yield and background values. As expected, larger deviations in the corrected yields were observed at low p_T , where the efficiencies are low and vary steeply with p_T , because of the tighter selections. Due to this, the systematic uncertainties are slightly larger in these p_T intervals. The assigned systematic uncertainty varies from 5% to 15% for D^0 , equals 10% for D^+ , and varies from 10% to 15% for D^{*+} .

A 5% systematic uncertainty related to the PID selection was evaluated by comparing the ratio of the corrected yields extracted with and without particle identification.

The uncertainty on the efficiencies arising from the difference between the real and simulated D-meson transverse momentum distributions depends on the width of the p_T intervals and on the variation of the efficiencies within them. This uncertainty also includes the effect of the p_T dependence of the nuclear modification factor. As explained in Section 3.2, for the centrality class 0–10%, the D-meson transverse momentum distribution from the PYTHIA simulation was re-weighted in order to reproduce the D^0 spectrum shape observed in data, while for the 30–50% centrality class, the weights were defined in order to match the p_T distributions from FONLL calculations multiplied by the R_{AA} from the BAMPS model. A systematic uncertainty was estimated by using two alternative D-meson p_T distributions in both centrality classes: i) FONLL p_T distributions, ii) FONLL p_T distributions multiplied by R_{AA} from the BAMPS model. In addition, for the most central events, a different parameterisation of the measured p_T spectrum was used. The resulting uncertainties decrease with increasing p_T , varying from 5–6% to 1% in the interval $2 < p_T < 36$ GeV/ c . For D^0 mesons, efficiencies increase by more than a factor five within the interval $1 < p_T < 2$ GeV/ c in the most central collisions. As a consequence, a larger uncertainty of 15% resulted from a detailed study of the stability of the corrected yields when changing the p_T spectrum in the simulation.

The systematic uncertainty on the subtraction of feed-down from B decays (i.e. the calculation of the f_{prompt} fraction) was estimated i) by varying the p_T -differential feed-down D-meson cross section from the FONLL calculation within the theoretical uncertainties, ii) by varying the hypothesis on the ratio of the prompt and feed-down D-meson R_{AA} in the range $1 < R_{AA}^{\text{feed-down}}/R_{AA}^{\text{prompt}} < 3$, and iii) by applying an alternative method to compute f_{prompt} . This second method is based on the ratio of charm and beauty FONLL cross sections, instead of the absolute beauty cross section. The procedure is the same used for previous measurements of D-meson production with ALICE [32, 35, 45]. The resulting uncertainty ranges between $^{+5}_{-45}\%$ at low p_T and $^{+3}_{-8}\%$ at high p_T for the 0–10% centrality class, and between $^{+5}_{-45}\%$ at low p_T and $^{+4}_{-8}\%$ at high p_T for the 30–50% centrality class. The uncertainty from the variation of the feed-down D-meson R_{AA} hypothesis ranges from 6 to 16%, as shown in Fig. 4, where the relative variation of the prompt D^0 yield is shown as a function of the hypothesis on $R_{AA}^{\text{feed-down}}/R_{AA}^{\text{prompt}}$ for four p_T intervals.

The uncertainties on the branching ratios were also considered [44] as well as the contribution due to the 1.1% uncertainty on the fraction of the hadronic cross section used in the Glauber fit to determine the centrality classes [39]. The latter was estimated from the variation of the D-meson dN/dp_T when the limits of the centrality classes are shifted by $\pm 1.1\%$ (e.g. shifted from 30–50% to 30.3–50.6% and 29.7–49.5%) [32]. The resulting uncertainty, common to all p_T intervals, is smaller than 1% for the 0–10% centrality class and about 2% for the 30–50% centrality class.

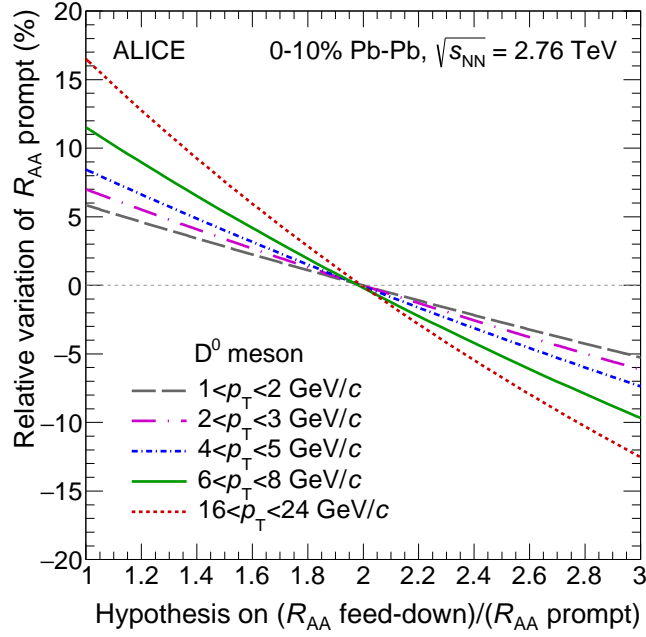


Figure 4: Relative variation of the prompt D^0 yields as a function of the hypothesis on $R_{AA}^{\text{feed-down}}/R_{AA}^{\text{prompt}}$ for the B-meson feed-down subtraction.

4.2 Systematic uncertainties on R_{AA}

The systematic uncertainties on the R_{AA} measurement include those on the D-meson corrected yields, those on the proton–proton cross section reference, and the uncertainties on the average nuclear overlap function.

The systematic uncertainties on the D-meson corrected yields are obtained considering as uncorrelated the different contributions described in the previous section.

The uncertainty on the pp reference used for the calculation of R_{AA} has two contributions. The first is the systematic uncertainty on the measured p_T -differential D-meson cross section at $\sqrt{s} = 7$ TeV. This uncertainty is about 25% at the lowest p_T and 17% at the highest p_T for D^0 mesons, excluding the uncertainty for feed-down corrections, and few percent larger for D^+ and D^{*+} mesons [45]. The systematic uncertainty on the feed-down subtraction deriving from the variation of the parameters of the FONLL calculation and from the use of the alternative method to compute f_{prompt} was considered to be correlated in the Pb–Pb and pp measurements. These variations were carried out simultaneously for the numerator and denominator of R_{AA} , so only the residual effect was attributed as a systematic uncertainty. Therefore, the variation of the value of $R_{AA}^{\text{feed-down}}/R_{AA}^{\text{prompt}}$ between 1 and 3 is the main contribution to the feed-down uncertainty on R_{AA} .

The second contribution to the pp reference uncertainty is the scaling to $\sqrt{s} = 2.76$ TeV. It ranges from $^{+27}_{-10}\%$ in the interval $2 < p_T < 3$ GeV/ c to about 5% for $p_T > 10$ GeV/ c [61]. Note that the upper/lower uncertainties are reversed when considering R_{AA} , where the pp reference is in the denominator. In the interval 1–2 GeV/ c , this scaling uncertainty is much larger ($^{+57}_{-11}\%$), but its impact on the pp reference was reduced by about a factor of two by using a weighted average of the cross section scaled from 7 TeV and the measured cross section at 2.76 TeV (see Section 3.2).

The extrapolation of the pp reference to the intervals $16 < p_T < 24$ GeV/ c for D^0 mesons and $24 < p_T < 36$ GeV/ c for D^+ and D^{*+} mesons resulted in a total systematic uncertainty of about $^{+35}_{-50}\%$, as described in Section 3.2.

Particle	D ⁰			D ⁺			D ^{*+}		
0–10% centrality class									
p_T interval (GeV/c)	1–2	6–8	16–24	3–4	6–8	24–36	3–4	6–8	24–36
$dN_{\text{Pb–Pb}}/dp_T$ (excl. feed-down)	28%	14%	22%	22%	20%	22%	24%	20%	21%
dN_{pp}/dp_T (excl. feed-down)	21%*	16%	17%	20%	19%	20%	17%	17%	18%
\sqrt{s} – scaling of the pp ref.	+6%* –30%*	+6% –10%	–	+8% –19%	+6% –10%	–	+9% –20%	+6% –10%	–
High- p_T extrapolation	–	–	+34% –51%	–	–	+37% –56%	–	–	+34% –53%
FONLL feed-down corr.	+1% –4%	+2% –4%	+10% –16%	+2% –1%	+1% –2%	+8% –14%	+1% –4%	+2% –4%	+3% –8%
$R_{\text{AA}}^{\text{feed-down}}/R_{\text{AA}}^{\text{prompt}}$ (Eq. (3))	+12% –9%	+14% –11%	+19% –13%	+8% –7%	+12% –9%	+16% –12%	+6% –6%	+8% –7%	+8% –7%
Normalisation	4.8%			4.8%			4.8%		
30–50% centrality class									
p_T interval (GeV/c)	1–2	6–8	12–16	2–3	6–8	12–16	2–3	6–8	12–16
$dN_{\text{Pb–Pb}}/dp_T$ (excl. feed-down)	20%	20%	22%	25%	21%	22%	29%	19%	18%
dN_{pp}/dp_T (excl. feed-down)	21%*	16%	17%	20%	19%	20%	17%	17%	18%
\sqrt{s} – scaling of the pp ref.	+6%* –30%*	+6% –10%	+5% –6%	+8% –19%	+6% –10%	+5% –6%	+9% –20%	+6% –10%	+5% –6%
FONLL feed-down corr.	+1% –5%	+2% –3%	+3% –4%	+1% –2%	+1% –3%	+3% –4%	+1% –2%	+3% –5%	+2% –3%
$R_{\text{AA}}^{\text{feed-down}}/R_{\text{AA}}^{\text{prompt}}$ (Eq. (3))	+12% –9%	+14% –11%	+15% –11%	+9% –7%	+13% –10%	+17% –13%	+7% –6%	+10% –8%	+9% –8%
Normalisation	6.2%			6.2%			6.2%		

Table 3: Relative systematic uncertainties on the prompt D-meson R_{AA} for three p_T intervals, in the two centrality classes. Uncertainties marked with a * were obtained as the average of the measurement at $\sqrt{s} = 2.76$ TeV and the measurement at $\sqrt{s} = 7$ TeV, scaled using FONLL [56], as described in Section 3.3.

The uncertainties on R_{AA} are listed in Tab. 3. The uncertainties on the normalisation are the quadratic sum of the pp normalisation uncertainty (3.5%) and the uncertainty on $\langle T_{\text{AA}} \rangle$, which is 3.2% and 4.7% in the 0–10% and 30–50% centrality classes, respectively.

All the uncertainties described in this Section that result from detector effects are considered to be largely correlated over transverse momentum, with the exception of the yield extraction uncertainty that depends on the S/B in each p_T interval. The uncertainties related to the feed-down assumptions and to the \sqrt{s} -scaled pp reference are fully correlated over p_T , with the exception of that for the hypothesis on the ratio of the prompt and feed-down D-meson R_{AA} that might not be constant as a function of p_T .

5 Results and discussion

5.1 D-meson p_T spectra and R_{AA}

The transverse momentum distributions dN/dp_T of prompt D⁰, D⁺ and D^{*+} mesons are shown in Figs. 5(a), 5(b) and 5(c) for the 10% most central Pb–Pb collisions. The results are presented in the interval $1 < p_T < 24$ GeV/c for the D⁰ mesons and $3 < p_T < 36$ GeV/c for D⁺ and D^{*+} mesons. They are compared to the corresponding pp cross section reference multiplied by $\langle T_{\text{AA}} \rangle$. The vertical bars represent the statistical uncertainties, the empty boxes the systematic uncertainties from the data analysis, and the shaded boxes the systematic uncertainty due to the subtraction of the feed-down from B-hadron decays. Uncertainties on the pp cross section normalisation and on the branching ratios are quoted separately. A clear suppression of the D-meson yields is observed at intermediate ($3 < p_T < 8$ GeV/c) and high transverse momenta ($p_T > 8$ GeV/c) in central Pb–Pb collisions as compared to the binary-scaled

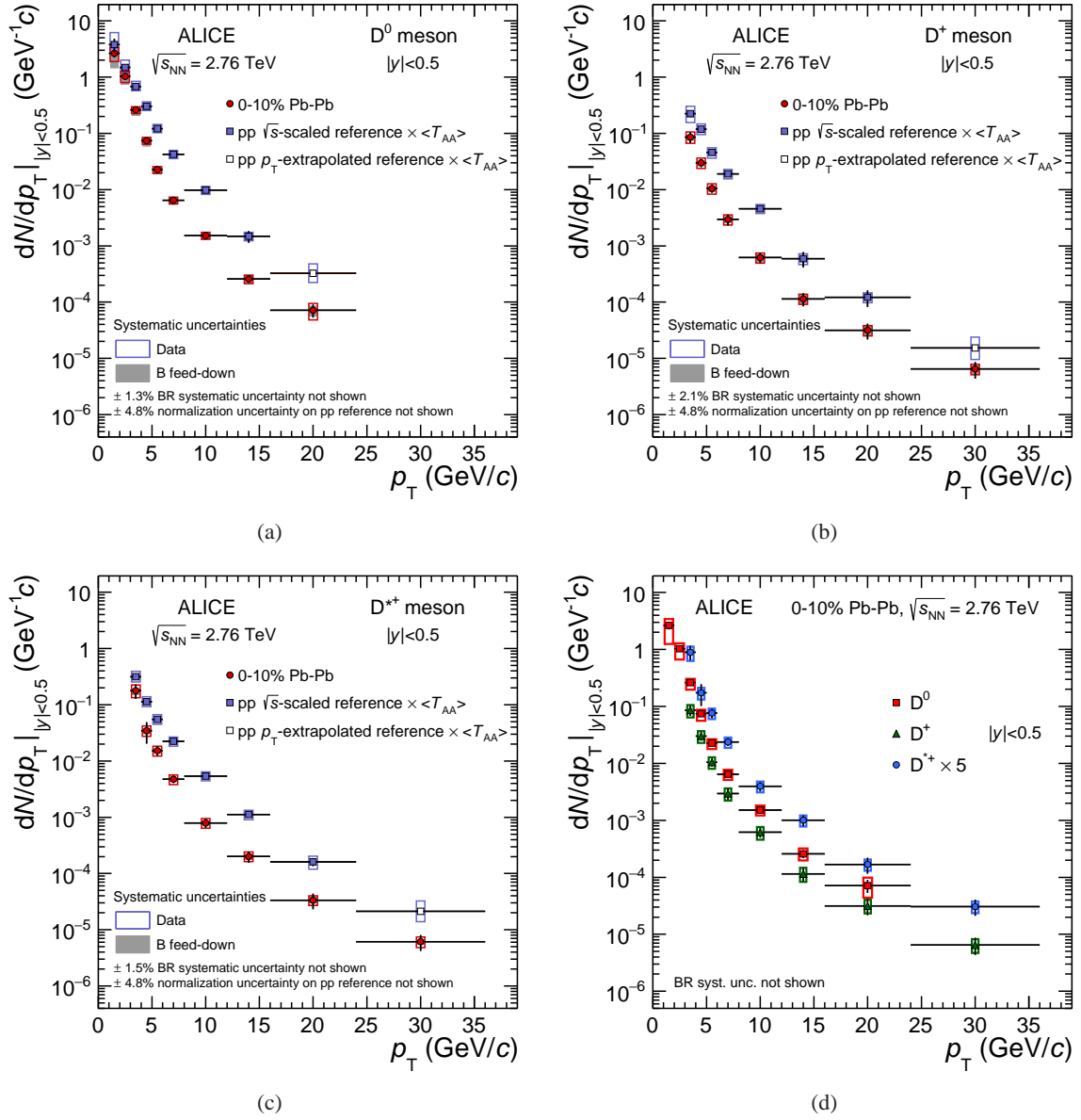


Figure 5: Transverse momentum distributions dN/dp_T of prompt D^0 (a), D^+ (b) and D^{*+} (c) mesons in the 0–10% centrality class in Pb–Pb collisions at $\sqrt{s_{NN}} = 2.76$ TeV. The pp reference distributions $\langle T_{AA} \rangle d\sigma/dp_T$ are shown as well. Statistical uncertainties (bars) and systematic uncertainties from data analysis (empty boxes) and from feed-down subtraction (shaded boxes) are shown. Horizontal bars represent bin widths, symbols are placed at the centre of the bin. The dN/dp_T distributions of the three D-meson species in the 10% most central Pb–Pb collisions are compared to each other in panel (d), where the D^{*+} production yields are scaled by a factor of five for visibility.

pp reference. In Fig. 5(d) the transverse momentum distributions of prompt D^0 , D^+ and D^{*+} mesons in the 10% most central collisions are compared to each other. The dN/dp_T values of D^{*+} mesons are scaled by a factor of five for visibility.

The D-meson dN/dp_T distributions measured in the 30–50% centrality class are shown in Fig. 6. Also for this centrality class, a clear suppression of the D-meson yields as compared to the expectation based on binary scaling of the pp yields is observed for $p_T > 3$ GeV/c. In Fig. 6(d), the dN/dp_T of prompt D^0 , D^+ and D^{*+} (the latter scaled by a factor of five) are compared to each other.

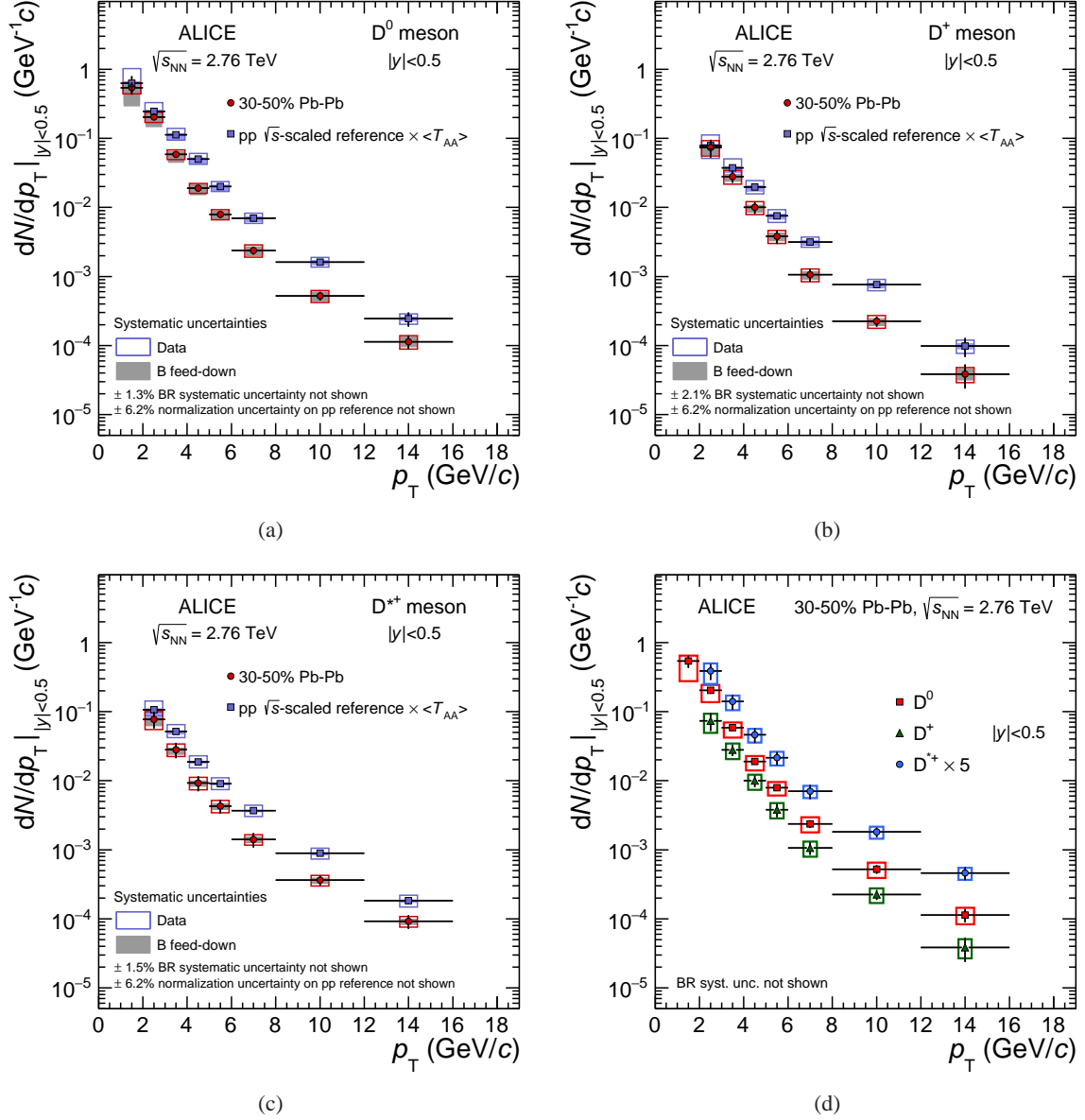


Figure 6: Transverse momentum distributions dN/dp_T of prompt D^0 (a), D^+ (b) and D^{*+} (c) mesons in the 30–50% centrality class in Pb–Pb collisions at $\sqrt{s_{NN}} = 2.76$ TeV. The pp reference distributions $\langle T_{AA} \rangle d\sigma/dp_T$ are shown as well. Statistical uncertainties (bars) and systematic uncertainties from data analysis (empty boxes) and from feed-down subtraction (shaded boxes) are shown. Horizontal bars represent bin widths, symbols are placed at the centre of the bin. The dN/dp_T distributions of the three D-meson species in Pb–Pb collisions in the 30–50% centrality class are compared to each other in panel (d), where the D^{*+} production yields are scaled by a factor of five for visibility.

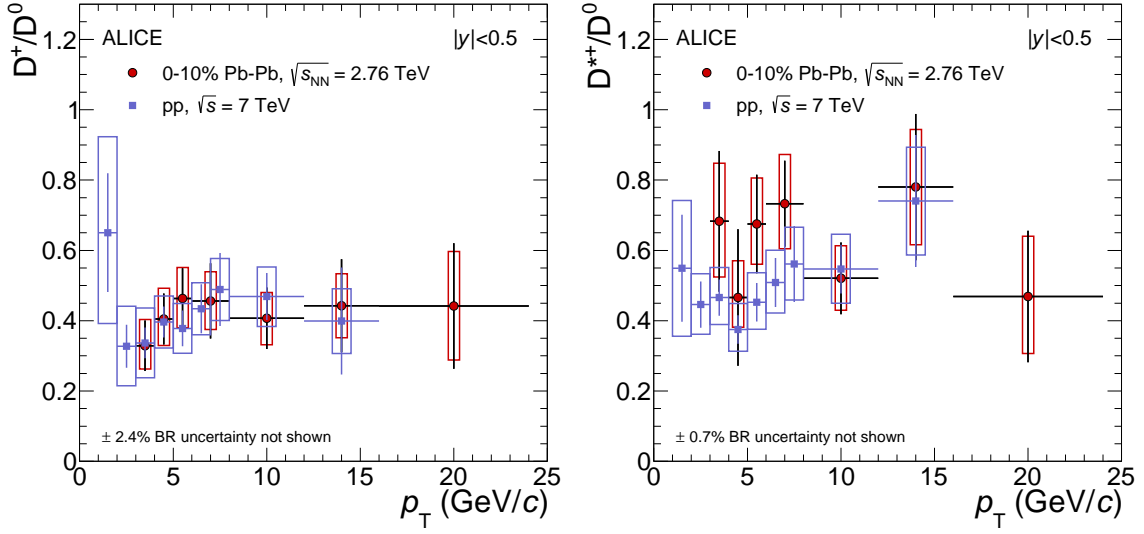


Figure 7: Ratio of prompt D-meson yields (D^+/D^0 and D^{*+}/D^0) as a function of p_T in the 10% most central Pb–Pb collisions at $\sqrt{s_{NN}} = 2.76$ TeV compared to the results in pp collisions at $\sqrt{s} = 7$ TeV. Statistical (bars) and systematic (boxes) uncertainties are shown.

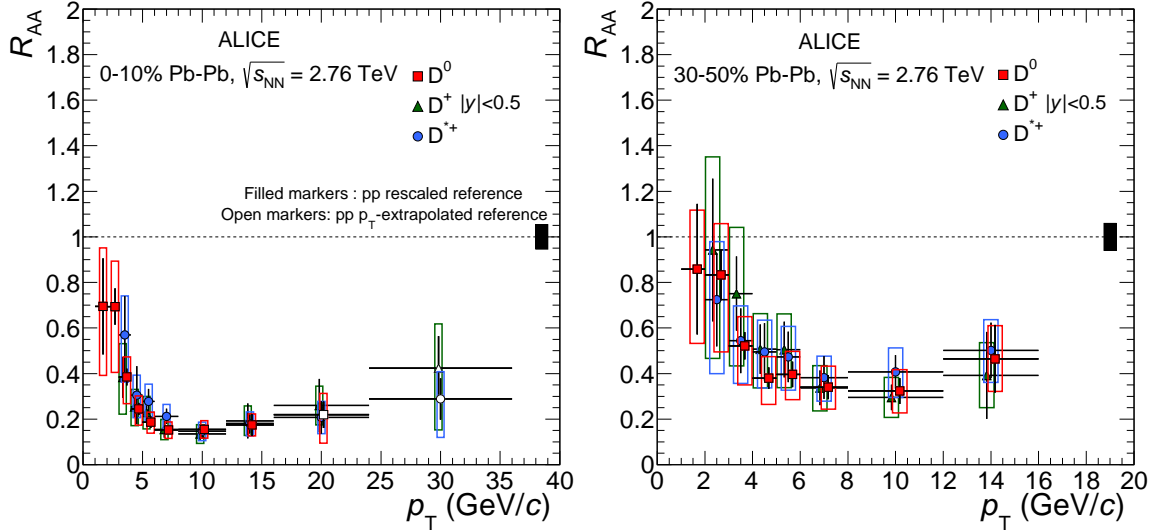


Figure 8: R_{AA} of prompt D^0 , D^+ , and D^{*+} mesons for the 0–10% (left) and 30–50% (right) centrality classes. Statistical (bars), systematic (empty boxes), and normalisation (shaded box) uncertainties are shown. Horizontal bars represent bin widths. D^0 symbols are placed at the centre of the bin. D^+ , and D^{*+} are shifted for visibility.

Figure 7 shows the p_T -dependent ratios of D^+/D^0 and D^{*+}/D^0 for central Pb–Pb collisions. They are found to be compatible within uncertainties with those measured in pp collisions at $\sqrt{s} = 7$ TeV [62]. Similar results were also found for the 30–50% centrality class. Therefore, no modification of the relative abundances of these three D-meson species is observed within the current uncertainties in central and semi-central Pb–Pb collisions relative to the pp ones at LHC energies.

The R_{AA} of prompt D^0 , D^+ and D^{*+} mesons is shown in Fig. 8 for the 0–10% (left panel) and 30–50% (right panel) centrality classes. The statistical uncertainties, represented by the vertical error bars, range from 10% in the intermediate p_T range up to about 25–30% in the lowest and highest p_T intervals, for the 10% most central collisions. The statistical uncertainty on the reference measurement at

$\sqrt{s} = 7$ TeV dominates this uncertainty in the interval $2 < p_T < 16$ GeV/ c . For the 30–50% centrality class, the statistical uncertainties at low and intermediate p_T are similar in magnitude to those of central collisions and are about 20% in the interval $12 < p_T < 16$ GeV/ c . The total p_T -dependent systematic uncertainties, described in the previous Section, are shown as empty boxes. The normalisation uncertainty is represented by a filled box at $R_{AA} = 1$. The nuclear modification factors of the three D-meson species are compatible within statistical uncertainties for both centrality classes. For the 10% most central collisions, the measured R_{AA} shows a suppression that is maximal at around $p_T = 10$ GeV/ c , where a reduction of the yields by a factor of 5–6 with respect to the binary-scaled pp reference is observed. The suppression decreases with decreasing p_T for $p_T < 10$ GeV/ c , and it is of the order of a factor of 3 in the interval $3 < p_T < 4$ GeV/ c , while the R_{AA} ranges from about 0.35 to 1 in the first two p_T intervals. For $p_T > 10$ GeV/ c , the suppression appears to decrease with increasing p_T , but the large statistical uncertainties do not allow us to determine the trend of the R_{AA} . A suppression ($R_{AA} < 0.5$) is still observed for D mesons with $p_T > 25$ GeV/ c . For the 30–50% centrality class, the suppression amounts to about a factor of 3 at $p_T = 10$ GeV/ c , which indicates that the suppression of the high- p_T D-meson yields is smaller than in the 0–10% centrality class. As for the central collisions, the suppression reduces at lower momenta, with R_{AA} increasing with decreasing p_T up to a value of about 0.6 in the interval $3 < p_T < 4$ GeV/ c . For lower p_T the suppression is further reduced and R_{AA} is compatible with unity.

The average nuclear modification factor of D^0 , D^+ and D^{*+} mesons was computed using the inverse of the squared relative statistical uncertainties as weights. The systematic uncertainties were propagated through the averaging procedure, considering the contributions from the tracking efficiency, the B-meson feed-down subtraction and the FONLL-based \sqrt{s} -scaling of the pp cross section from $\sqrt{s} = 7$ TeV to $\sqrt{s} = 2.76$ TeV as fully correlated uncertainties among the three D-meson species. The average D-meson R_{AA} for the two centrality classes is shown in the left panel of Fig. 9. A larger suppression, by about a factor of two, is observed in the 10% most central collisions compared to the 30–50% centrality class for $p_T > 5$ GeV/ c . The stronger suppression observed in central collisions can be understood as resulting from the increasing medium density, size and lifetime from peripheral to central collisions. The R_{AA} values measured for the 0–10% centrality class are slightly lower, although compatible within uncertainties, than those reported in Ref. [32] for the 20% most central collisions, measured with the 2010 data sample. As a consistency check, the analysis on the 2011 data sample was also performed in the 0–20% centrality class and the resulting R_{AA} value was found to be compatible with the one measured with the 2010 sample within statistical and systematic uncertainties, considering that the pp reference uncertainties are the same in the two measurements. In addition, the larger sample of central Pb–Pb collisions used in this analysis, compared to that used in the previous publication, enables the measurement of the D-meson R_{AA} in a wider p_T range (the intervals $1 < p_T < 2$ GeV/ c and $p_T > 16$ GeV/ c were not accessible with the previous sample), with a substantial reduction (by a factor of about 2–3) of the statistical uncertainties.

Figure 9 (left) also shows the average D-meson nuclear modification factor measured in minimum-bias p–Pb collisions at $\sqrt{s_{NN}} = 5.02$ TeV [33]. Since no significant modification of the D-meson production is observed in p–Pb collisions for $p_T > 2$ GeV/ c , the strong suppression of the D-meson yields for $p_T > 3$ GeV/ c observed in central and semi-central Pb–Pb collisions cannot be explained in terms of cold nuclear matter effects and is predominantly due to final-state effects induced by the hot and dense medium created in the collisions.

5.2 Comparison with results at lower collision energy

In the right panel of Fig. 9, the average D-meson R_{AA} for the 10% most central Pb–Pb collisions is compared to the D^0 nuclear modification factor measured by the STAR Collaboration for the 10% most central Au–Au collisions at $\sqrt{s_{NN}} = 200$ GeV [31]. The D-meson R_{AA} measured at the two energies are compatible within uncertainties for $p_T > 2$ GeV/ c . It should be noted that the similar R_{AA} of D mesons with high momentum, $p_T > 5$ GeV/ c , i.e. in the range where the nuclear modification factor is

expected to be dominated by the effect of in-medium parton energy loss, does not necessarily imply a similar charm-quark energy loss at the two collision energies. Since the nuclear modification factor is also sensitive to the slope of the p_T spectra in pp collisions, the combined effect of a denser medium and of the harder p_T spectra at the LHC could result in similar values of R_{AA} as at lower collision energies (see e.g. Ref. [63]).

At low momentum ($1 < p_T < 2$ GeV/ c), the R_{AA} measured by STAR shows a maximum. This effect can be described by models including parton energy loss, collective radial flow and the contribution of the recombination mechanism to charm-quark hadronisation [30]. The ALICE results at higher $\sqrt{s_{NN}}$ do not show a maximum. However, the large uncertainties and the coarser binning at low p_T prevent a firm conclusion from being drawn. A different pattern could be explained by the different role of initial-state effects or of radial flow at the two collision energies. In the initial state, the modification of the parton distribution functions in a nuclear environment is predicted to lead to a stronger suppression of the heavy-quark production yields at low p_T with increasing $\sqrt{s_{NN}}$ [64], because of the smaller values of Bjorken- x probed. In addition, the momentum (k_T) broadening effect, which gives rise to an enhancement of the R_{AA} at intermediate p_T (Cronin peak), is known to be more pronounced at lower collision energies [65, 66]. In the final state, in addition to energy loss, the collective expansion of the medium is also predicted to affect the momentum distribution of charmed hadrons in heavy-ion collisions. Indeed, the interactions with the medium constituents are expected to transfer momentum to low- p_T charm quarks, which could take part in the collective radial flow of the medium. This effect could be enhanced by hadronisation via recombination, which is predicted in some models to contribute significantly to hadron formation at low and intermediate p_T [15]. The momentum distributions of identified light-flavour hadrons at the LHC [67, 68] indicate that the radial flow of the medium at LHC energies is about 10% higher than at RHIC [69]. However, this stronger radial flow does not necessarily give rise to a more pronounced bump-like structure in the R_{AA} at low p_T with increasing collision energy, because its effect can be counterbalanced by the different shape of the momentum spectra in pp collisions at different \sqrt{s} [70, 71].

5.3 Comparison with pion and charged-hadron R_{AA}

As described in Section 1, the colour-charge and quark-mass dependence of the energy loss can be tested with the comparison of D-meson and pion nuclear modification factors. In the left panel of Fig. 10, the D-meson R_{AA} (average of D^0 , D^+ and D^{*+}) measured for the 10% most central Pb–Pb collisions is compared with the pion R_{AA} in the interval $1 < p_T < 20$ GeV/ c and with the R_{AA} of charged particles in $16 < p_T < 40$ GeV/ c . The charged-particle R_{AA} is shown in order to extend the comparison up to the higher p_T interval in which the D-meson yield was measured. The comparison of D mesons with charged hadrons at high- p_T is relevant because the R_{AA} of different light-flavour hadron species are consistent with one another for $p_T > 8$ GeV/ c [72]. Moreover the contribution of pions dominates the charged-hadron yields at p_T of about 20 GeV/ c with respect to other hadron species (about 65%) [74]. A similar comparison is performed in the right panel of Fig. 10 for the 30–50% centrality class.

The R_{AA} of D mesons and light-flavour hadrons are consistent for $p_T > 6$ GeV/ c for both centrality classes. For $p_T < 6$ GeV/ c , the R_{AA} of D mesons tends to be slightly higher than that of pions. This can be also observed from the ratio of nuclear modification factors, presented in Fig. 13. Considering that the systematic uncertainties of D-meson yields are mainly correlated with p_T , we observe $R_{AA}^D > R_{AA}^\pi$ at low p_T with a significance of about 1σ in four p_T intervals, in the most central events. In the 30–50% centrality class, the significance of the effect is smaller than in central collisions.

A direct interpretation of a possible difference between the D-meson and pion R_{AA} at low p_T is not straightforward. In the presence of a colour-charge and quark-mass dependent energy loss, the harder p_T distribution and the harder fragmentation function of charm quarks compared to those of light quarks and gluons could lead to similar values of D-meson and pion R_{AA} , as discussed in Ref. [13]. In addition, it should be considered that the pion yield could have a substantial contribution from soft production pro-

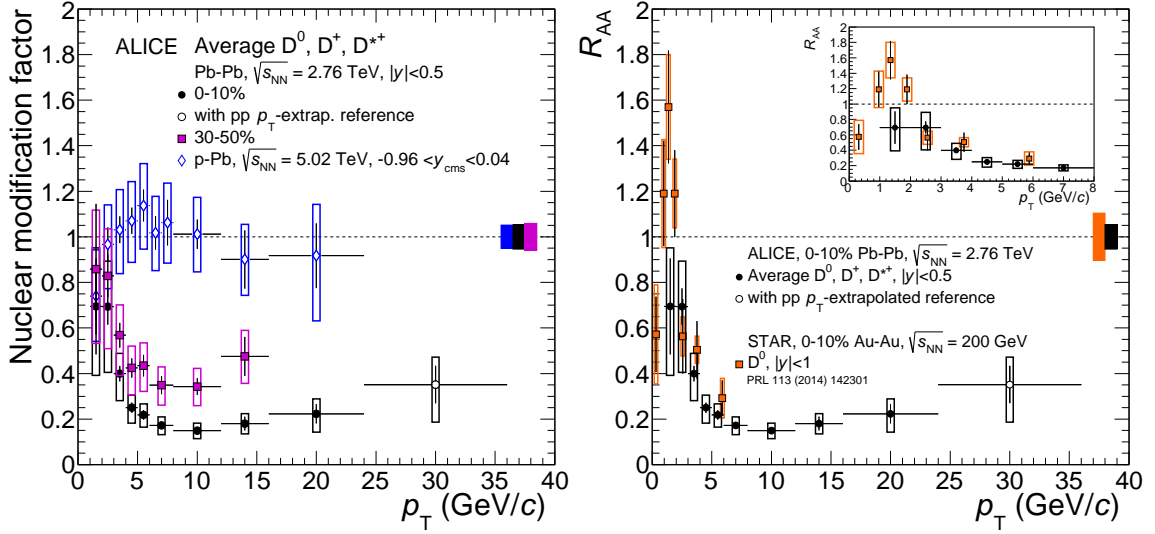


Figure 9: Left: prompt D-meson R_{AA} (average of D^0 , D^+ and D^{*+}) as a function of p_T in Pb–Pb collisions at $\sqrt{s_{NN}} = 2.76$ TeV in the 0–10% and 30–50% centrality classes. Prompt D-meson nuclear modification factor (average of D^0 , D^+ and D^{*+}) as a function of p_T in p–Pb collisions at $\sqrt{s_{NN}} = 5.02$ TeV [33]. Right: prompt D-meson R_{AA} (average of D^0 , D^+ and D^{*+}) as a function of p_T in the 10% most central Pb–Pb collisions at $\sqrt{s_{NN}} = 2.76$ TeV compared to D^0 R_{AA} measured by the STAR Collaboration in Au–Au collisions at RHIC at $\sqrt{s_{NN}} = 200$ GeV [31]. A zoomed-in plot of the interval $0 < p_T < 8$ GeV/c is shown in the inset. Statistical (bars), systematic (empty boxes), and normalisation (shaded boxes at $R_{AA} = 1$) uncertainties are shown. Horizontal bars represent bin widths. Symbols are placed at the centre of the bin.

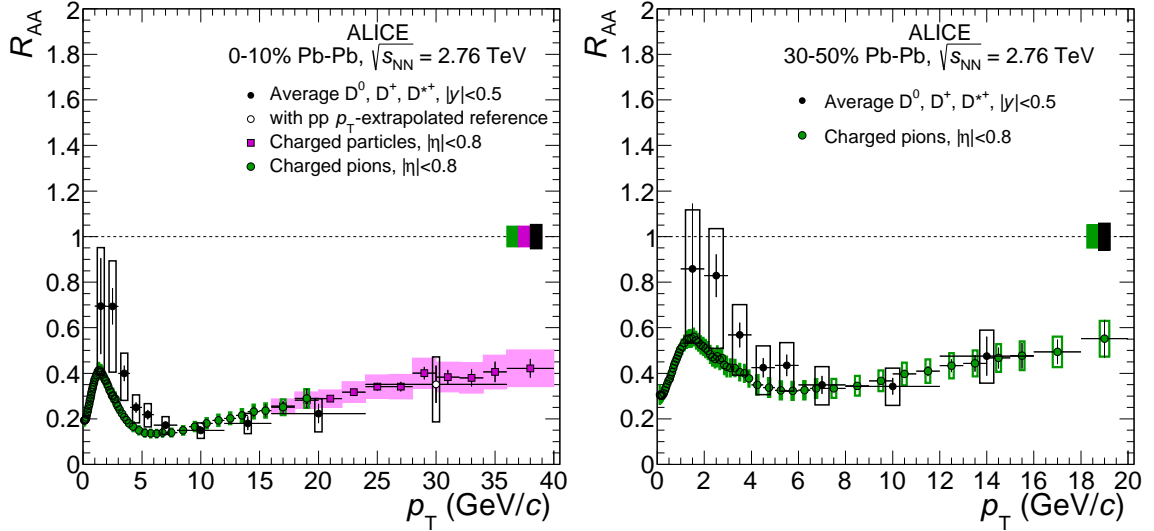


Figure 10: Prompt D-meson R_{AA} (average of D^0 , D^+ and D^{*+}) as a function of p_T compared to the nuclear modification factors of pions [72] and charged particles [73] in the 0–10% (left) and 30–50% (right) centrality classes. Statistical (bars), systematic (empty boxes), and normalisation (shaded box at $R_{AA} = 1$) uncertainties are shown. Horizontal bars represent bin widths. Symbols are placed at the centre of the bin.

cesses up to transverse momenta of about 2–3 GeV/c due to the strong radial flow at LHC energies. This soft contribution, which is not present in the D-meson yield, does not scale with the number of binary nucleon–nucleon collisions. Finally, the effects of radial flow and hadronisation via recombination, as

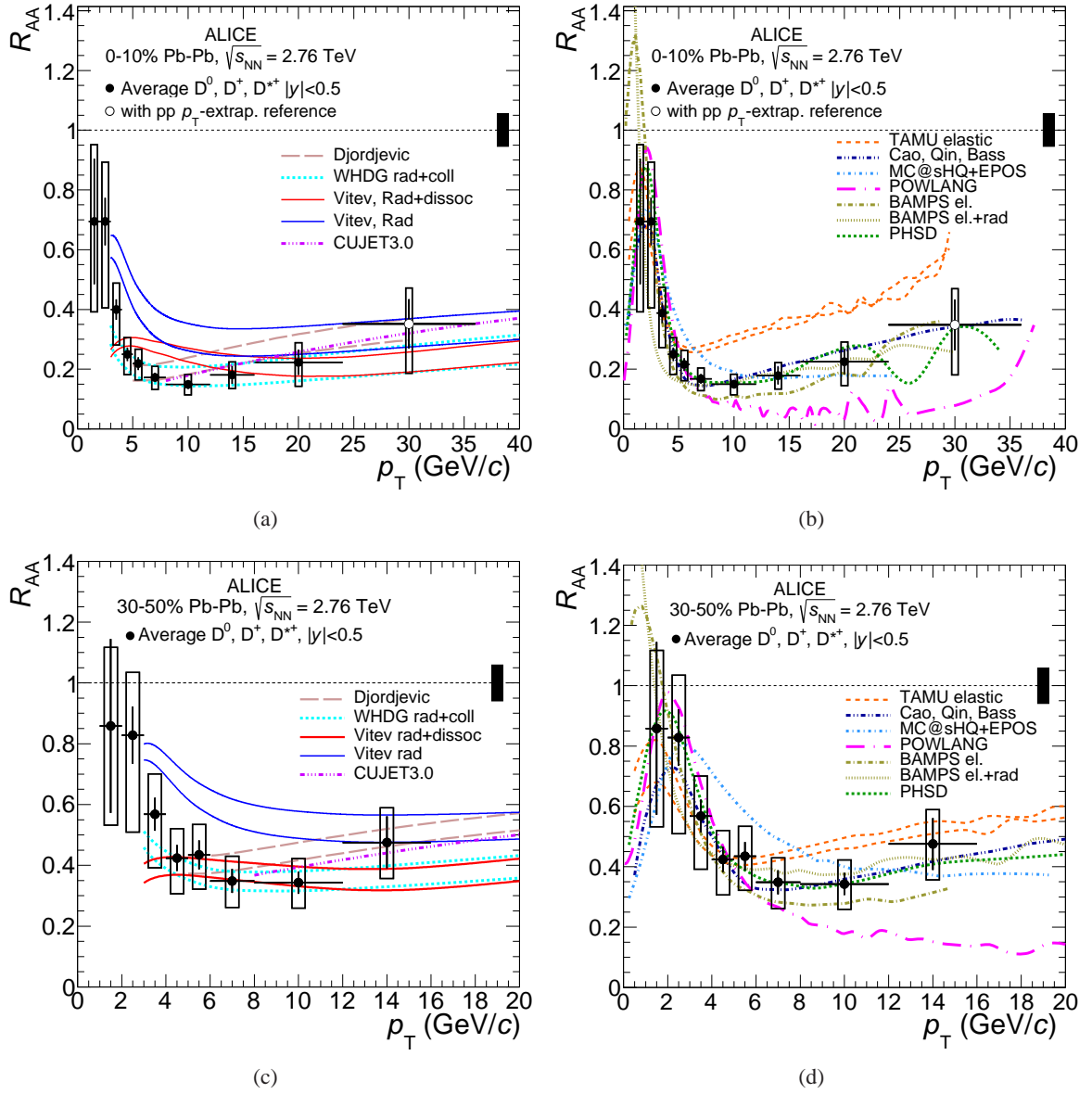


Figure 11: Average of prompt D^0 , D^+ and D^{*+} R_{AA} in the centrality classes 0–10% (a and b) and 30–50% (c and d) compared with model calculations: *Djordjevic* [75], *CUJET3.0* [76, 77], *WHDG* [20–22], *Vitev* [78] (a and c), *TAMU elastic* [70], *Cao, Qin and Bass* [79], *MC@sHQ+EPOS*, *Coll+Rad(LPM)* [80], *POWLANG* [81, 82], *BAMPS* [53–55], *PHSD* [83] (b and d). Some of the model calculations are shown by two lines to represent their uncertainties.

well as initial-state effects, could affect D-meson and pion (light-flavour particle) yields differently at a given p_T , thus introducing an additional complication in interpreting the magnitude of the R_{AA} in terms of different in-medium parton energy loss of charm quarks, light quarks and gluons.

5.4 Comparison with models

Figure 11 shows the comparison of the average D-meson R_{AA} for the two centrality classes 0–10% (a and b) and 30–50% (c and d) with most of the available model calculations. The model calculations are described and compared in a recent review [15]. A concise summary is given in the following paragraphs.

The interaction of heavy quarks with the medium constituents is computed considering radiative and

collisional processes in the calculations indicated as *Djordjevic* [75], *WHDG* [20–22], *CUJET3.0* [76, 77], *MC@shQ+EPOS* [80], *BAMPS* [53–55], and *Cao, Qin, Bass* [79]. Only collisional interactions are considered in the model calculations *POWLANG* [81, 82], *TAMU elastic* [70] and *PHSD* [83]. In *BAMPS*, two different options are considered: including only collisional energy loss but introducing a scaling factor to match RHIC high- p_T data (where radiative energy loss is expected to be dominant) or including both collisional and radiative energy loss. Also for the *Vitev* model [78] two different options are considered: including only radiative energy loss (*Vitev rad*) or also considering the in-medium dissociation of heavy-flavour hadrons (*Vitev rad+dissoc*).

The medium is described using an underlying hydrodynamical model in *CUJET3.0*, *Cao, Qin, Bass*, *MC@shQ+EPOS*, *BAMPS*, *POWLANG*, *TAMU elastic* and *PHSD*, while *Djordjevic*, *WHDG* and *Vitev* use a Glauber model nuclear overlap without radial expansion.

The initial heavy-quark p_T distributions are based on next-to-leading order (NLO) or FONLL perturbative QCD calculations in all model calculations, except for *Cao, Qin, Bass*, which uses the PYTHIA event generator [49]. The EPS09 NLO parameterisation [64] of the nuclear parton distribution functions is included by *POWLANG*, *MC@shQ+EPOS*, *TAMU elastic*, *PHSD* and *Cao, Qin, Bass*.

All model calculations use in-vacuum fragmentation of heavy quarks for the high-momentum region. At low momentum this is supplemented by hadronisation via recombination in the *MC@shQ+EPOS*, *POWLANG*², *Cao, Qin, Bass*, *TAMU elastic* and *PHSD* models. The two last models also include scattering of D mesons in the hadronic phase of the medium. Also for the *Cao, Qin, Bass* model, the hadronic-rescattering effects have been studied in a recent publication [84] and no large differences in the R_{AA} are observed, when these processes are considered.

Several model calculations provide a good description of the measured R_{AA} for both centrality classes. The *MC@shQ+EPOS* model has recently improved the description of the R_{AA} in the p_T interval 2–8 GeV/ c including the EPS09 shadowing parameterisation in addition to in-medium energy loss, the *TAMU elastic* model overestimates the R_{AA} in central collisions in the p_T interval 6–30 GeV/ c and the *POWLANG* model underestimates it in the interval 5–36 (8–16) GeV/ c in the 0–10% (30–50%) centrality class. Interestingly, these model calculations provide a fair description of the D-meson v_2 measured at LHC [35] and of the D-meson R_{AA} measured at RHIC [31]. On the other hand, the model calculations that do not include a hydrodynamical medium expansion and hadronisation via recombination, namely *Djordjevic*, *Vitev*, *WHDG*—and as a consequence do not describe the features observed for the v_2 at the LHC and the R_{AA} at RHIC in the momentum region up to about 3–5 GeV/ c —provide a good description of the R_{AA} in the full “high p_T interval”, above 5 GeV/ c . The *Vitev* model shows a better agreement when including the D-meson in-medium dissociation mechanism. The *BAMPS* model with collisional energy loss describes the data better for the low- p_T interval, as is the case for the D-meson v_2 [35]. The inclusion of radiative energy loss improves the agreement at high p_T . The *Cao, Qin, Bass* model describes the R_{AA} in both centrality classes, but underestimates the D-meson v_2 [35]. The *PHSD* model describes the R_{AA} in both centrality classes.

Figure 12 shows the *TAMU elastic* and *MC@shQ+EPOS* calculations of the nuclear modification factor, for the 10% most central events, with and without including the EPS09 shadowing parameterisation. For both models the inclusion of shadowing reduces the R_{AA} by up to about 30–40% in the interval $p_T < 5$ GeV/ c , resulting in a better description of the data.

Four of the model calculations also provide the nuclear modification factor of pions and charged particles (*Djordjevic*, *CUJET3.0*, *WHDG* and *Vitev*). All these calculations include radiative and collisional energy loss³. The left panel of Fig. 13 shows the comparison with the measured charged-pion R_{AA}^π ($p_T <$

²Note that recombination was not included in the version of the *POWLANG* model used for the comparison with the D-meson v_2 measurement in [35].

³The in-medium formation and dissociation process, included by *Vitev* for D mesons, is not relevant for pions, which have

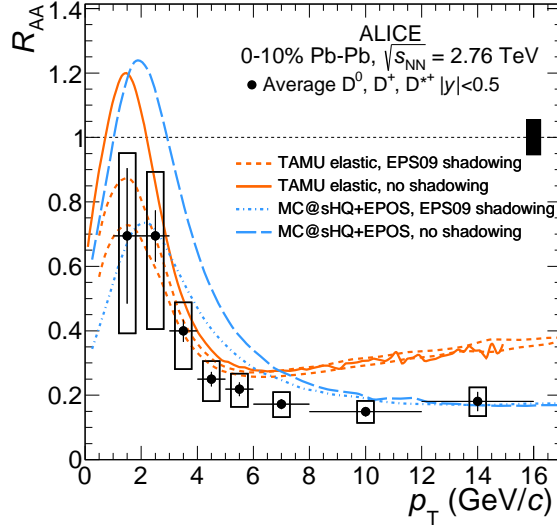


Figure 12: Average of prompt D^0 , D^+ and D^{*+} R_{AA} in the centrality classes 0–10% compared with $TAMU$ elastic and $MC@sHQ+EPOS$ models calculations with and without including EPS09 shadowing parameterisations [64].

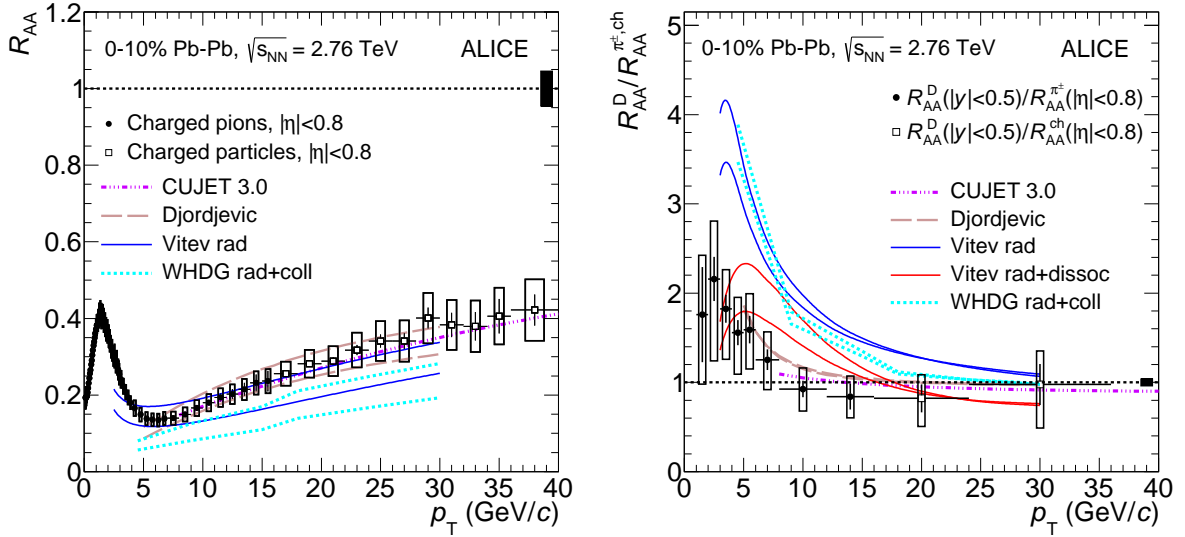


Figure 13: Left: R_{AA} of charged pions ($p_T < 16$ GeV/c) [72] and of charged particles ($p_T > 16$ GeV/c) [73] compared with model calculations that compute also the D-meson R_{AA} . Right: ratio of the R_{AA} of prompt D mesons (average of D^0 , D^+ and D^{*+} as shown in Fig. 11) and the R_{AA} of charged pions (for $p_T < 20$ GeV/c) or charged particles (for $p_T > 20$ GeV/c), compared with the same model calculations shown in the left panel.

16 GeV/c) [72] and charged-particle R_{AA}^{ch} ($p_T > 16$ GeV/c) [73]. The model calculations provide a reasonable description of the measurements, with $WHDG$ generally showing smaller R_{AA} values than seen in data, although consistent within experimental and theoretical uncertainties.

The right panel of Fig. 13 shows the $R_{AA}^D / R_{AA}^{\pi^+, ch}$ ($p_T < 16$ GeV/c) and R_{AA}^D / R_{AA}^{ch} ($p_T > 16$ GeV/c) ratios for data and for these four model calculations. In the case of data, the uncertainties of D-meson and charged-pion (or charged-particle) measurements were propagated as uncorrelated uncertainties, except

a much larger formation time.

for the uncertainty on $\langle T_{AA} \rangle$, which cancels in the ratio⁴. In the case of model calculations, the theoretical uncertainty, when provided, was propagated assuming full correlation between D mesons and pions (charged particles), since it accounts for a variation of the medium density (or temperature). Only the *Djordjevic* and *CUJET3.0* models, which use radiative and collisional energy loss, can describe the two R_{AA} results and their ratio over the full p_T interval in which they provide the calculations ($p_T > 5$ and 8 GeV/c, respectively). The *Vitev* model can describe the data at the lowest p_T (2–6 GeV/c) only if the dissociation mechanism is included, suggesting that the effect is relevant in this model. However, the model overestimates the data in the interval 6–12 GeV/c.

6 Conclusions

We have presented the measurements of the production of prompt D^0 , D^+ and D^{*+} mesons at central rapidity in Pb–Pb collisions at a centre-of-mass energy per nucleon pair $\sqrt{s_{NN}} = 2.76$ TeV, as well as their nuclear modification factor R_{AA} . The measurements cover the interval $1 < p_T < 36$ GeV/c for the 0–10% centrality class and $1 < p_T < 16$ GeV/c for the 30–50% centrality class.

The nuclear modification factor shows a maximum reduction of the yields with respect to binary scaling by a factor 5–6, for transverse momenta of about 10 GeV/c for the 10% most central Pb–Pb collisions. A suppression of a factor about 2–3 persists in the highest p_T interval covered by the measurements (24–36 GeV/c). At low p_T (1–3 GeV/c), the R_{AA} has large uncertainties, that span the range from 0.35 (factor of three suppression) to 1 (no suppression). In all p_T intervals above 5 GeV/c, the R_{AA} for the 30–50% centrality class is about twice that for the 0–10% centrality class. The suppression observed for $p_T > 3$ GeV/c is interpreted to be due to interactions of the charm quarks within the high-energy density medium formed in the final-state of Pb–Pb collisions. This is demonstrated by the nuclear modification factor measurements in p–Pb collisions at $\sqrt{s_{NN}} = 5.02$ TeV, which indicate that D-meson production is consistent with binary collision scaling [33].

The D-meson R_{AA} was compared with that of charged pions in the interval $1 < p_T < 16$ GeV/c, also in terms of the ratio R_{AA}^D/R_{AA}^π , and with that of charged particles up to $p_T = 36$ GeV/c (R_{AA}^D/R_{AA}^{ch}). In the interval $1 < p_T < 6$ GeV/c, the R_{AA} values of D mesons are higher than those of pions, although consistent within uncertainties. For the 10% most central collisions, the ratio $R_{AA}^D/R_{AA}^{\pi, ch}$ is larger than unity by about 1σ of the total uncertainties, which are to some extent correlated among p_T intervals. For $p_T > 8$ GeV/c, the R_{AA} values are compatible with those of pions and charged particles up to $p_T = 36$ GeV/c.

Several models provide a good description of the R_{AA} for both centrality classes. Interestingly, the models that show larger deviation from the data, especially in the high- p_T region, are among those that provide a good description of the D-meson v_2 measured at the LHC and of the D-meson R_{AA} measured at RHIC, in the low- p_T region. On the other hand, the models that do not include a hydrodynamical medium expansion and recombination, and as a consequence do not describe v_2 in the momentum region up to about 3–5 GeV/c, provide a good description of the R_{AA} at the LHC in the full high- p_T interval, above 5 GeV/c.

Only two out of the four models that compute $R_{AA}^D/R_{AA}^{\pi, ch}$ can describe this measurement over the full p_T interval for which they provide the calculations. In these models, the nuclear modification factors of D mesons and pions turn out to be very similar as a consequence of a compensation among the larger energy loss of gluons with respect to that of charm quarks (mainly due to the larger colour coupling factor), the different amount of gluon and light quark yields on the pion R_{AA} and the harder p_T distribution and fragmentation of charm quarks with respect to those of gluons and of light quarks.

⁴The uncertainty on the normalisation (integrated luminosity) of the pp reference cross sections for D mesons and pions (charged particles) does not cancel in the ratio, because the two cross sections were measured in two data samples at different centre-of-mass energies.

Acknowledgements

The ALICE Collaboration would like to thank all its engineers and technicians for their invaluable contributions to the construction of the experiment and the CERN accelerator teams for the outstanding performance of the LHC complex. The ALICE Collaboration gratefully acknowledges the resources and support provided by all Grid centres and the Worldwide LHC Computing Grid (WLCG) collaboration. The ALICE Collaboration acknowledges the following funding agencies for their support in building and running the ALICE detector: State Committee of Science, World Federation of Scientists (WFS) and Swiss Fonds Kidagan, Armenia; Conselho Nacional de Desenvolvimento Científico e Tecnológico (CNPq), Financiadora de Estudos e Projetos (FINEP), Fundação de Amparo à Pesquisa do Estado de São Paulo (FAPESP); National Natural Science Foundation of China (NSFC), the Chinese Ministry of Education (CMOE) and the Ministry of Science and Technology of China (MSTC); Ministry of Education and Youth of the Czech Republic; Danish Natural Science Research Council, the Carlsberg Foundation and the Danish National Research Foundation; The European Research Council under the European Community's Seventh Framework Programme; Helsinki Institute of Physics and the Academy of Finland; French CNRS-IN2P3, the 'Region Pays de Loire', 'Region Alsace', 'Region Auvergne' and CEA, France; German Bundesministerium für Bildung, Wissenschaft, Forschung und Technologie (BMBF) and the Helmholtz Association; General Secretariat for Research and Technology, Ministry of Development, Greece; Hungarian Országos Tudományos Kutatási Alapprogramok (OTKA) and National Office for Research and Technology (NKTH); Department of Atomic Energy and Department of Science and Technology of the Government of India; Istituto Nazionale di Fisica Nucleare (INFN) and Centro Fermi - Museo Storico della Fisica e Centro Studi e Ricerche "Enrico Fermi", Italy; MEXT Grant-in-Aid for Specially Promoted Research, Japan; Joint Institute for Nuclear Research, Dubna; National Research Foundation of Korea (NRF); Consejo Nacional de Ciencia y Tecnología (CONACYT), Dirección General de Asuntos del Personal Académico (DGAPA), México, Amérique Latine Formation académique - European Commission (ALFA-EC) and the EPLANET Program (European Particle Physics Latin American Network); Stichting voor Fundamenteel Onderzoek der Materie (FOM) and the Nederlandse Organisatie voor Wetenschappelijk Onderzoek (NWO), Netherlands; Research Council of Norway (NFR); National Science Centre, Poland; Ministry of National Education/Institute for Atomic Physics and National Council of Scientific Research in Higher Education (CNCSI-UEFISCDI), Romania; Ministry of Education and Science of Russian Federation, Russian Academy of Sciences, Russian Federal Agency of Atomic Energy, Russian Federal Agency for Science and Innovations and The Russian Foundation for Basic Research; Ministry of Education of Slovakia; Department of Science and Technology, South Africa; Centro de Investigaciones Energéticas, Medioambientales y Tecnológicas (CIEMAT), E-Infrastructure shared between Europe and Latin America (EELA), Ministerio de Economía y Competitividad (MINECO) of Spain, Xunta de Galicia (Consellería de Educación), Centro de Aplicaciones Tecnológicas y Desarrollo Nuclear (CEADEN), Cubaenergía, Cuba, and IAEA (International Atomic Energy Agency); Swedish Research Council (VR) and Knut & Alice Wallenberg Foundation (KAW); Ukraine Ministry of Education and Science; United Kingdom Science and Technology Facilities Council (STFC); The United States Department of Energy, the United States National Science Foundation, the State of Texas, and the State of Ohio; Ministry of Science, Education and Sports of Croatia and Unity through Knowledge Fund, Croatia; Council of Scientific and Industrial Research (CSIR), New Delhi, India; Pontificia Universidad Católica del Perú.

References

- [1] F. Karsch, “Lattice simulations of the thermodynamics of strongly interacting elementary particles and the exploration of new phases of matter in relativistic heavy ion collisions,” *J.Phys.Conf.Ser.* **46** (2006) 122–131, arXiv:hep-lat/0608003 [hep-lat].
- [2] **Wuppertal-Budapest** Collaboration, S. Borsanyi *et al.*, “Is there still any T_c mystery in lattice QCD? Results with physical masses in the continuum limit III,” *JHEP* **1009** (2010) 073, arXiv:1005.3508 [hep-lat].
- [3] S. Borsanyi, Z. Fodor, C. Hoelbling, S. D. Katz, S. Krieg, *et al.*, “Full result for the QCD equation of state with 2+1 flavors,” *Phys.Lett.* **B730** (2014) 99–104, arXiv:1309.5258 [hep-lat].
- [4] A. Bazavov, T. Bhattacharya, M. Cheng, C. DeTar, H. Ding, *et al.*, “The chiral and deconfinement aspects of the QCD transition,” *Phys.Rev.* **D85** (2012) 054503, arXiv:1111.1710 [hep-lat].
- [5] F.-M. Liu and S.-X. Liu, “Quark-gluon plasma formation time and direct photons from heavy ion collisions,” *Phys. Rev.* **C89** no. 3, (2014) 034906, arXiv:1212.6587 [nucl-th].
- [6] M. Gyulassy and M. Plumer, “Jet Quenching in Dense Matter,” *Phys.Lett.* **B243** (1990) 432–438.
- [7] R. Baier, Y. L. Dokshitzer, A. H. Mueller, S. Peigne, and D. Schiff, “Radiative energy loss and $p(T)$ broadening of high-energy partons in nuclei,” *Nucl.Phys.* **B484** (1997) 265–282, arXiv:hep-ph/9608322 [hep-ph].
- [8] M. H. Thoma and M. Gyulassy, “Quark Damping and Energy Loss in the High Temperature QCD,” *Nucl.Phys.* **B351** (1991) 491–506.
- [9] E. Braaten and M. H. Thoma, “Energy loss of a heavy fermion in a hot plasma,” *Phys.Rev.* **D44** (1991) 1298–1310.
- [10] E. Braaten and M. H. Thoma, “Energy loss of a heavy quark in the quark - gluon plasma,” *Phys.Rev.* **D44** (1991) 2625–2630.
- [11] R. Glauber and G. Matthiae, “High-energy scattering of protons by nuclei,” *Nucl.Phys.* **B21** (1970) 135–157.
- [12] M. L. Miller, K. Reygers, S. J. Sanders, and P. Steinberg, “Glauber modeling in high energy nuclear collisions,” *Ann.Rev.Nucl.Part.Sci.* **57** (2007) 205–243, arXiv:nucl-ex/0701025 [nucl-ex].
- [13] M. Djordjevic, “Heavy flavor puzzle at LHC: a serendipitous interplay of jet suppression and fragmentation,” *Phys.Rev.Lett.* **112** no. 4, (2014) 042302, arXiv:1307.4702 [nucl-th].
- [14] N. Armesto, A. Dainese, C. A. Salgado, and U. A. Wiedemann, “Testing the color charge and mass dependence of parton energy loss with heavy-to-light ratios at RHIC and CERN LHC,” *Phys.Rev.* **D71** (2005) 054027, arXiv:hep-ph/0501225 [hep-ph].
- [15] A. Andronic, F. Arleo, R. Arnaldi, A. Beraudo, E. Bruna, *et al.*, “Heavy-flavour and quarkonium production in the LHC era: from proton-proton to heavy-ion collisions,” arXiv:1506.03981 [nucl-ex].
- [16] Y. L. Dokshitzer and D. Kharzeev, “Heavy quark colorimetry of QCD matter,” *Phys.Lett.* **B519** (2001) 199–206, arXiv:hep-ph/0106202 [hep-ph].
- [17] N. Armesto, C. A. Salgado, and U. A. Wiedemann, “Medium induced gluon radiation off massive quarks fills the dead cone,” *Phys.Rev.* **D69** (2004) 114003, arXiv:hep-ph/0312106 [hep-ph].

- [18] M. Djordjevic and M. Gyulassy, “Heavy quark radiative energy loss in QCD matter,” *Nucl.Phys.* **A733** (2004) 265–298, arXiv:nucl-th/0310076 [nucl-th].
- [19] B.-W. Zhang, E. Wang, and X.-N. Wang, “Heavy quark energy loss in nuclear medium,” *Phys.Rev.Lett.* **93** (2004) 072301, arXiv:nucl-th/0309040 [nucl-th].
- [20] S. Wicks, W. Horowitz, M. Djordjevic, and M. Gyulassy, “Elastic, inelastic, and path length fluctuations in jet tomography,” *Nucl.Phys.* **A784** (2007) 426–442, arXiv:nucl-th/0512076 [nucl-th].
- [21] W. Horowitz and M. Gyulassy, “The Surprising Transparency of the sQGP at LHC,” *Nucl.Phys.* **A872** (2011) 265–285, arXiv:1104.4958 [hep-ph].
- [22] W. Horowitz, “Testing pQCD and AdS/CFT Energy Loss at RHIC and LHC,” *AIP Conf.Proc.* **1441** (2012) 889–891, arXiv:1108.5876 [hep-ph].
- [23] H. van Hees, V. Greco, and R. Rapp, “Heavy-quark probes of the quark-gluon plasma at RHIC,” *Phys.Rev.* **C73** (2006) 034913, arXiv:nucl-th/0508055 [nucl-th].
- [24] S. Batsouli, S. Kelly, M. Gyulassy, and J. L. Nagle, “Does the charm flow at RHIC?,” *Phys. Lett.* **B557** (2003) 26–32, arXiv:nucl-th/0212068 [nucl-th].
- [25] V. Greco, C. M. Ko, and R. Rapp, “Quark coalescence for charmed mesons in ultrarelativistic heavy ion collisions,” *Phys. Lett.* **B595** (2004) 202–208, arXiv:nucl-th/0312100 [nucl-th].
- [26] A. Andronic, P. Braun-Munzinger, K. Redlich, and J. Stachel, “Statistical hadronization of charm in heavy ion collisions at SPS, RHIC and LHC,” *Phys. Lett.* **B571** (2003) 36–44, arXiv:nucl-th/0303036 [nucl-th].
- [27] **PHENIX** Collaboration, S. Adler *et al.*, “Nuclear modification of electron spectra and implications for heavy quark energy loss in Au+Au collisions at $\sqrt{s_{NN}} = 200$ GeV,” *Phys.Rev.Lett.* **96** (2006) 032301, arXiv:nucl-ex/0510047 [nucl-ex].
- [28] **PHENIX** Collaboration, A. Adare *et al.*, “Heavy Quark Production in $p + p$ and Energy Loss and Flow of Heavy Quarks in Au+Au Collisions at $\sqrt{s_{NN}} = 200$ GeV,” *Phys.Rev.* **C84** (2011) 044905, arXiv:1005.1627 [nucl-ex].
- [29] **PHENIX** Collaboration, A. Adare *et al.*, “Nuclear-Modification Factor for Open-Heavy-Flavor Production at Forward Rapidity in Cu+Cu Collisions at $\sqrt{s_{NN}} = 200$ GeV,” *Phys.Rev.* **C86** (2012) 024909, arXiv:1204.0754 [nucl-ex].
- [30] **STAR** Collaboration, B. Abelev *et al.*, “Transverse momentum and centrality dependence of high- p_T non-photonic electron suppression in Au+Au collisions at $\sqrt{s_{NN}} = 200$ GeV,” *Phys.Rev.Lett.* **98** (2007) 192301, arXiv:nucl-ex/0607012 [nucl-ex].
- [31] **STAR** Collaboration, L. Adamczyk *et al.*, “Observation of D^0 Meson Nuclear Modifications in Au+Au Collisions at $\sqrt{s_{NN}} = 200$ GeV,” *Phys.Rev.Lett.* **113** no. 14, (2014) 142301, arXiv:1404.6185 [nucl-ex].
- [32] **ALICE** Collaboration, B. Abelev *et al.*, “Suppression of high transverse momentum D mesons in central Pb-Pb collisions at $\sqrt{s_{NN}} = 2.76$ TeV,” *JHEP* **1209** (2012) 112, arXiv:1203.2160 [nucl-ex].
- [33] **ALICE** Collaboration, B. Abelev *et al.*, “Measurement of prompt D-meson production in $p - Pb$ collisions at $\sqrt{s_{NN}} = 5.02$ TeV,” *Phys.Rev.Lett.* **113** no. 23, (2014) 232301, arXiv:1405.3452 [nucl-ex].

- [34] **ALICE** Collaboration, B. Abelev *et al.*, “D meson elliptic flow in non-central Pb-Pb collisions at $\sqrt{s_{NN}} = 2.76\text{TeV}$,” *Phys.Rev.Lett.* **111** (2013) 102301, arXiv:1305.2707 [nucl-ex].
- [35] **ALICE** Collaboration, B. Abelev *et al.*, “Azimuthal anisotropy of D meson production in Pb-Pb collisions at $\sqrt{s_{NN}} = 2.76\text{ TeV}$,” *Phys.Rev.* **C90** no. 3, (2014) 034904, arXiv:1405.2001 [nucl-ex].
- [36] **ALICE** Collaboration, K. Aamodt *et al.*, “The ALICE experiment at the CERN LHC,” *JINST* **3** (2008) S08002.
- [37] **ALICE** Collaboration, B. Abelev *et al.*, “Performance of the ALICE Experiment at the CERN LHC,” *Int.J.Mod.Phys.* **A29** (2014) 1430044, arXiv:1402.4476 [nucl-ex].
- [38] **ALICE** Collaboration, E. Abbas *et al.*, “Performance of the ALICE VZERO system,” *JINST* **8** (2013) P10016, arXiv:1306.3130 [nucl-ex].
- [39] **ALICE** Collaboration, B. Abelev *et al.*, “Centrality determination of Pb-Pb collisions at $\sqrt{s_{NN}} = 2.76\text{ TeV}$ with ALICE,” *Phys.Rev.* **C88** no. 4, (2013) 044909, arXiv:1301.4361 [nucl-ex].
- [40] R. Fruhwirth, “Application of Kalman filtering to track and vertex fitting,” *Nucl.Instrum.Meth.* **A262** (1987) 444–450.
- [41] **ALICE** Collaboration, J. Alme *et al.*, “The ALICE TPC, a large 3-dimensional tracking device with fast readout for ultra-high multiplicity events,” *Nuclear Instruments and Methods in Physics Research Section A: Accelerators, Spectrometers, Detectors and Assocs*
- [42] **ALICE** Collaboration, K. Aamodt *et al.*, “Alignment of the ALICE Inner Tracking System with cosmic-ray tracks,” *JINST* **5** (2010) P03003, arXiv:1001.0502 [physics.ins-det].
- [43] A. Akindinov *et al.*, “Performance of the ALICE Time-Of-Flight detector at the LHC,” *Eur. Phys. J. Plus* **128** (2013) 44.
- [44] **Particle Data Group** Collaboration, K. Olive *et al.*, “Review of Particle Physics,” *Chin.Phys.* **C38** (2014) 090001.
- [45] **ALICE** Collaboration, B. Abelev *et al.*, “Measurement of charm production at central rapidity in proton-proton collisions at $\sqrt{s} = 7\text{ TeV}$,” *JHEP* **1201** (2012) 128, arXiv:1111.1553 [hep-ex].
- [46] P. Z. Skands, “The Perugia Tunes,” *FERMILAB-CONF-09-113-T*, arXiv:0905.3418 [hep-ph] (2009) 284–297, arXiv:0905.3418 [hep-ph].
- [47] R. Brun, F. Carminati, and S. Giani, “CERN Program Library Long Write-up, W5013 GEANT Detector Description and Simulation Tool,”.
- [48] X.-N. Wang and M. Gyulassy, “HIJING: A Monte Carlo model for multiple jet production in p p, p A and A A collisions,” *Phys.Rev.* **D44** (1991) 3501–3516.
- [49] T. Sjostrand, S. Mrenna, and P. Z. Skands, “PYTHIA 6.4 Physics and Manual,” *JHEP* **0605** (2006) 026, arXiv:hep-ph/0603175 [hep-ph].
- [50] P. Z. Skands, “Tuning Monte Carlo Generators: The Perugia Tunes,” *Phys.Rev.* **D82** (2010) 074018, arXiv:1005.3457 [hep-ph].
- [51] M. Cacciari, M. Greco, and P. Nason, “The P(T) spectrum in heavy flavor hadroproduction,” *JHEP* **9805** (1998) 007, arXiv:hep-ph/9803400 [hep-ph].

- [52] M. Cacciari, S. Frixione, and P. Nason, “The p_T spectrum in heavy flavor photoproduction,” *JHEP* **0103** (2001) 006, arXiv:hep-ph/0102134 [hep-ph].
- [53] J. Uphoff, O. Fochler, Z. Xu, and C. Greiner, “Elliptic Flow and Energy Loss of Heavy Quarks in Ultra-Relativistic heavy Ion Collisions,” *Phys.Rev.* **C84** (2011) 024908, arXiv:1104.2295 [hep-ph].
- [54] O. Fochler, J. Uphoff, Z. Xu, and C. Greiner, “Jet quenching and elliptic flow at RHIC and LHC within a pQCD-based partonic transport model,” *J.Phys.* **G38** (2011) 124152, arXiv:1107.0130 [hep-ph].
- [55] J. Uphoff, O. Fochler, Z. Xu, and C. Greiner, “Open Heavy Flavor in Pb+Pb Collisions at $\sqrt{s} = 2.76$ TeV within a Transport Model,” *Phys.Lett.* **B717** (2012) 430–435, arXiv:1205.4945 [hep-ph].
- [56] M. Cacciari, S. Frixione, N. Houdeau, M. L. Mangano, P. Nason, *et al.*, “Theoretical predictions for charm and bottom production at the LHC,” *JHEP* **1210** (2012) 137, arXiv:1205.6344 [hep-ph].
- [57] D. J. Lange, “The evtgen particle decay simulation package,” *Nuclear Instruments and Methods in Physics Research Section A: Accelerators, Spectrometers, Detectors and Assocs* BEAUTY2000, Proceedings of the 7th Int. Conf. on B-Physics at Hadron Machines.
- [58] ALICE Collaboration, J. Adam *et al.*, “Centrality dependence of high- p_T D meson suppression in Pb-Pb collisions at $\sqrt{s_{NN}} = 2.76$ TeV,” arXiv:1506.06604 [nucl-ex].
- [59] CMS Collaboration, CMS, “J/psi results from CMS in PbPb collisions, with 150mub-1 data,” CMS-PAS-HIN-12-014.
- [60] ALICE Collaboration, B. Abelev *et al.*, “Measurement of charm production at central rapidity in proton-proton collisions at $\sqrt{s} = 2.76$ TeV,” *JHEP* **1207** (2012) 191, arXiv:1205.4007 [hep-ex].
- [61] Z. Conesa del Valle, G. Corcella, F. Fleuret, E. G. Ferreira, V. Kartvelishvili, *et al.*, “Quarkonium production in high energy proton-proton and proton-nucleus collisions,” *Nucl.Phys.Proc.Suppl.* **214** (2011) 3–36, arXiv:1105.4545 [hep-ph].
- [62] ALICE Collaboration, B. Abelev *et al.*, “ D_s^+ meson production at central rapidity in proton–proton collisions at $\sqrt{s} = 7$ TeV,” *Phys.Lett.* **B718** (2012) 279–294, arXiv:1208.1948 [hep-ex].
- [63] R. Baier, “Jet quenching,” *Nucl. Phys.* **A715** (2003) 209–218, arXiv:hep-ph/0209038 [hep-ph].
- [64] K. Eskola, H. Paukkunen, and C. Salgado, “EPS09: A New Generation of NLO and LO Nuclear Parton Distribution Functions,” *JHEP* **0904** (2009) 065, arXiv:0902.4154 [hep-ph].
- [65] X.-N. Wang, “Systematic study of high p_T hadron spectra in pp , pA and AA collisions from SPS to RHIC energies,” *Phys.Rev.* **C61** (2000) 064910, arXiv:nucl-th/9812021 [nucl-th].
- [66] Hard Probe Collaboration, R. Vogt, “The A dependence of open charm and bottom production,” *Int.J.Mod.Phys.* **E12** (2003) 211–270, arXiv:hep-ph/0111271 [hep-ph].
- [67] ALICE Collaboration, B. Abelev *et al.*, “Pion, Kaon, and Proton Production in Central Pb–Pb Collisions at $\sqrt{s_{NN}} = 2.76$ TeV,” *Phys.Rev.Lett.* **109** (2012) 252301, arXiv:1208.1974 [hep-ex].

- [68] **ALICE** Collaboration, B. Abelev *et al.*, “Centrality dependence of π , K, p production in Pb–Pb collisions at $\sqrt{s_{NN}} = 2.76$ TeV,” *Phys.Rev.* **C88** (2013) 044910, arXiv:1303.0737 [hep-ex].
- [69] **STAR** Collaboration, B. Abelev *et al.*, “Systematic Measurements of Identified Particle Spectra in pp , d+Au and Au+Au Collisions from STAR,” *Phys.Rev.* **C79** (2009) 034909, arXiv:0808.2041 [nucl-ex].
- [70] M. He, R. J. Fries, and R. Rapp, “Heavy Flavor at the Large Hadron Collider in a Strong Coupling Approach,” *Phys.Lett.* **B735** (2014) 445–450, arXiv:1401.3817 [nucl-th].
- [71] M. He, R. J. Fries, and R. Rapp, “Heavy-Quark Diffusion and Hadronization in Quark-Gluon Plasma,” *Phys. Rev.* **C86** (2012) 014903, arXiv:1106.6006 [nucl-th].
- [72] **ALICE** Collaboration, B. Abelev *et al.*, “Production of charged pions, kaons and protons at large transverse momenta in pp and PbPb collisions at $\sqrt{s_{NN}} = 2.76$ TeV,” *Phys.Lett.* **B736** (2014) 196–207, arXiv:1401.1250 [nucl-ex].
- [73] **ALICE** Collaboration, B. Abelev *et al.*, “Centrality Dependence of Charged Particle Production at Large Transverse Momentum in Pb–Pb Collisions at $\sqrt{s_{NN}} = 2.76$ TeV,” *Phys.Lett.* **B720** (2013) 52–62, arXiv:1208.2711 [hep-ex].
- [74] **ALICE** Collaboration, J. Adam *et al.*, “Centrality dependence of the nuclear modification factor of charged pions, kaons, and protons in Pb–Pb collisions at $\sqrt{s_{NN}} = 2.76$ TeV,” arXiv:1506.07287 [nucl-ex].
- [75] M. Djordjevic, M. Djordjevic, and B. Blagojevic, “RHIC and LHC jet suppression in non-central collisions,” *Phys.Lett.* **B737** (2014) 298–302, arXiv:1405.4250 [nucl-th].
- [76] J. Xu, J. Liao, and M. Gyulassy, “Consistency of Perfect Fluidity and Jet Quenching in semi-Quark-Gluon Monopole Plasmas,” *Chin. Phys. Lett.* **32** no. 9, (2015) 092501, arXiv:1411.3673 [hep-ph].
- [77] J. Xu, J. Liao, and M. Gyulassy, “Robustness and Consistency of Jet Quenching and Perfect Fluidity in semi Quark Gluon Monopole Plasmas (sQGMP) Produced at RHIC and LHC,” arXiv:1508.00552 [hep-ph].
- [78] R. Sharma, I. Vitev, and B.-W. Zhang, “Light-cone wave function approach to open heavy flavor dynamics in QCD matter,” *Phys.Rev.* **C80** (2009) 054902, arXiv:0904.0032 [hep-ph].
- [79] S. Cao, G.-Y. Qin, and S. A. Bass, “Heavy-quark dynamics and hadronization in ultrarelativistic heavy-ion collisions: Collisional versus radiative energy loss,” *Phys.Rev.* **C88** no. 4, (2013) 044907, arXiv:1308.0617 [nucl-th].
- [80] M. Nahrgang, J. Aichelin, P. B. Gossiaux, and K. Werner, “Influence of hadronic bound states above T_c on heavy-quark observables in Pb + Pb collisions at the CERN Large Hadron Collider,” *Phys.Rev.* **C89** no. 1, (2014) 014905, arXiv:1305.6544 [hep-ph].
- [81] W. Alberico, A. Beraudo, A. De Pace, A. Molinari, M. Monteno, *et al.*, “Heavy-flavour spectra in high energy nucleus-nucleus collisions,” *Eur.Phys.J.* **C71** (2011) 1666, arXiv:1101.6008 [hep-ph].
- [82] A. Beraudo, A. De Pace, M. Monteno, M. Nardi, and F. Prino, “Heavy flavors in heavy-ion collisions: quenching, flow and correlations,” *Eur. Phys. J.* **C75** no. 3, (2015) 121, arXiv:1410.6082 [hep-ph].

- [83] T. Song, H. Berrehrah, D. Cabrera, W. Cassing, and E. Bratkovskaya, “Charm production in Pb+Pb collisions at the Large Hadron Collider energy,” arXiv:1512.00891 [nucl-th].
- [84] S. Cao, G.-Y. Qin, and S. A. Bass, “Energy loss, hadronization and hadronic interactions of heavy flavors in relativistic heavy-ion collisions,” *Phys. Rev.* **C92** no. 2, (2015) 024907, arXiv:1505.01413 [nucl-th].

A The ALICE Collaboration

J. Adam⁴⁰, D. Adamová⁸³, M.M. Aggarwal⁸⁷, G. Aglieri Rinella³⁶, M. Agnello¹¹⁰, N. Agrawal⁴⁸,
 Z. Ahammed¹³², S.U. Ahn⁶⁸, S. Aiola¹³⁶, A. Akindinov⁵⁸, S.N. Alam¹³², D. Aleksandrov⁹⁹, B. Alessandro¹¹⁰,
 D. Alexandre¹⁰¹, R. Alfaro Molina⁶⁴, A. Alici^{12,104}, A. Alkin³, J.R.M. Almaraz¹¹⁹, J. Alme³⁸, T. Alt⁴³,
 S. Altinpinar¹⁸, I. Altsybeev¹³¹, C. Alves Garcia Prado¹²⁰, C. Andrei⁷⁸, A. Andronic⁹⁶, V. Anguelov⁹³,
 J. Anielski⁵⁴, T. Antičić⁹⁷, F. Antinori¹⁰⁷, P. Antonioli¹⁰⁴, L. Aphecetche¹¹³, H. Appelshäuser⁵³, S. Arcelli²⁸,
 R. Arnaldi¹¹⁰, O.W. Arnold^{37,92}, I.C. Arsene²², M. Arslandok⁵³, B. Audurier¹¹³, A. Augustinus³⁶,
 R. Averbeck⁹⁶, M.D. Azmi¹⁹, A. Badalà¹⁰⁶, Y.W. Baek^{67,44}, S. Bagnasco¹¹⁰, R. Bailhache⁵³, R. Bala⁹⁰,
 A. Baldisseri¹⁵, R.C. Baral⁶¹, A.M. Barbano²⁷, R. Barbera²⁹, F. Barile³³, G.G. Barnaföldi¹³⁵, L.S. Barnby¹⁰¹,
 V. Barret⁷⁰, P. Bartalini⁷, K. Barth³⁶, J. Bartke¹¹⁷, E. Bartsch⁵³, M. Basile²⁸, N. Bastid⁷⁰, S. Basu¹³²,
 B. Bathen⁵⁴, G. Batigne¹¹³, A. Batista Camejo⁷⁰, B. Batyunya⁶⁶, P.C. Batzing²², I.G. Bearden⁸⁰, H. Beck⁵³,
 C. Bedda¹¹⁰, N.K. Behera⁵⁰, I. Belikov⁵⁵, F. Bellini²⁸, H. Bello Martinez², R. Bellwied¹²², R. Belmont¹³⁴,
 E. Belmont-Moreno⁶⁴, V. Belyaev⁷⁵, G. Bencedi¹³⁵, S. Beole²⁷, I. Berceau⁷⁸, A. Bercuci⁷⁸, Y. Berdnikov⁸⁵,
 D. Berenyi¹³⁵, R.A. Bertens⁵⁷, D. Berzano³⁶, L. Betev³⁶, A. Bhasin⁹⁰, I.R. Bhat⁹⁰, A.K. Bhati⁸⁷,
 B. Bhattacharjee⁴⁵, J. Bhom¹²⁸, L. Bianchi¹²², N. Bianchi⁷², C. Bianchin^{57,134}, J. Bielčič⁴⁰, J. Bielčiková⁸³,
 A. Bilandžić⁸⁰, R. Biswas⁴, S. Biswas⁷⁹, S. Bjelogrić⁵⁷, J.T. Blair¹¹⁸, D. Blau⁹⁹, C. Blume⁵³, F. Bock^{93,74},
 A. Bogdanov⁷⁵, H. Bøggild⁸⁰, L. Boldizsár¹³⁵, M. Bombara⁴¹, J. Book⁵³, H. Borel¹⁵, A. Borissov⁹⁵,
 M. Borri^{82,124}, F. Bossú⁶⁵, E. Botta²⁷, S. Böttger⁵², C. Bourjau⁸⁰, P. Braun-Munzinger⁹⁶, M. Bregant¹²⁰,
 T. Breitner⁵², T.A. Broker⁵³, T.A. Browning⁹⁴, M. Broz⁴⁰, E.J. Brucken⁴⁶, E. Bruna¹¹⁰, G.E. Bruno³³,
 D. Budnikov⁹⁸, H. Buesching⁵³, S. Bufalino^{27,36}, P. Buncic³⁶, O. Busch^{93,128}, Z. Buthelezi⁶⁵, J.B. Butt¹⁶,
 J.T. Buxton²⁰, D. Caffarri³⁶, X. Cai⁷, H. Caines¹³⁶, L. Calero Diaz⁷², A. Caliva⁵⁷, E. Calvo Villar¹⁰²,
 P. Camerini²⁶, F. Carena³⁶, W. Carena³⁶, F. Carnesecchi²⁸, J. Castillo Castellanos¹⁵, A.J. Castro¹²⁵,
 E.A.R. Casula²⁵, C. Ceballos Sanchez⁹, J. Cepila⁴⁰, P. Cerello¹¹⁰, J. Cercala¹¹⁵, B. Chang¹²³, S. Chapeland³⁶,
 M. Chartier¹²⁴, J.L. Charvet¹⁵, S. Chattopadhyay¹³², S. Chattopadhyay¹⁰⁰, V. Chelnokov³, M. Cherney⁸⁶,
 C. Cheshkov¹³⁰, B. Cheynis¹³⁰, V. Chibante Barroso³⁶, D.D. Chinellato¹²¹, S. Cho⁵⁰, P. Chochula³⁶,
 K. Choi⁹⁵, M. Chojnacki⁸⁰, S. Choudhury¹³², P. Christakoglou⁸¹, C.H. Christensen⁸⁰, P. Christiansen³⁴,
 T. Chujo¹²⁸, S.U. Chung⁹⁵, C. Cicalo¹⁰⁵, L. Cifarelli^{12,28}, F. Cindolo¹⁰⁴, J. Cleymans⁸⁹, F. Colamaria³³,
 D. Colella^{33,36}, A. Collu^{74,25}, M. Colocci²⁸, G. Conesa Balbastre⁷¹, Z. Conesa del Valle⁵¹,
 M.E. Connors^{ii,136}, J.G. Contreras⁴⁰, T.M. Cormier⁸⁴, Y. Corrales Morales¹¹⁰, I. Cortés Maldonado²,
 P. Cortese³², M.R. Cosentino¹²⁰, F. Costa³⁶, P. Crochet⁷⁰, R. Cruz Albino¹¹, E. Cuautle⁶³, L. Cunqueiro³⁶,
 T. Dahms^{92,37}, A. Dainese¹⁰⁷, A. Danu⁶², D. Das¹⁰⁰, I. Das^{51,100}, S. Das⁴, A. Dash^{121,79}, S. Dash⁴⁸,
 S. De¹²⁰, A. De Caro^{31,12}, G. de Cataldo¹⁰³, C. de Conti¹²⁰, J. de Cuveland⁴³, A. De Falco²⁵, D. De
 Gruttola^{12,31}, N. De Marco¹¹⁰, S. De Pasquale³¹, A. Deisting^{96,93}, A. Deloff⁷⁷, E. Dénes^{135,i}, C. Deplano⁸¹,
 P. Dhankher⁴⁸, D. Di Bari³³, A. Di Mauro³⁶, P. Di Nezza⁷², M.A. Diaz Corchero¹⁰, T. Dietel⁸⁹,
 P. Dillenseger⁵³, R. Diviá³⁶, Ø. Djuvsland¹⁸, A. Dobrin^{57,81}, D. Domenicis Gimenez¹²⁰, B. Dönigus⁵³,
 O. Dordic²², T. Drozhzhova⁵³, A.K. Dubey¹³², A. Dubla⁵⁷, L. Ducroux¹³⁰, P. Dupieux⁷⁰, R.J. Ehlers¹³⁶,
 D. Elia¹⁰³, H. Engel⁵², E. Epple¹³⁶, B. Erazmus¹¹³, I. Erdemir⁵³, F. Erhardt¹²⁹, B. Espagnon⁵¹,
 M. Estienne¹¹³, S. Esumi¹²⁸, J. Eum⁹⁵, D. Evans¹⁰¹, S. Evdokimov¹¹¹, G. Eyyubova⁴⁰, L. Fabbietti^{92,37},
 D. Fabris¹⁰⁷, J. Faivre⁷¹, A. Fantoni⁷², M. Fasel⁷⁴, L. Feldkamp⁵⁴, A. Feliciello¹¹⁰, G. Feofilov¹³¹,
 J. Ferencei⁸³, A. Fernández Téllez², E.G. Ferreira¹⁷, A. Ferretti²⁷, A. Festanti³⁰, V.J.G. Feuillard^{15,70},
 J. Figiel¹¹⁷, M.A.S. Figueredo^{124,120}, S. Filchagin⁹⁸, D. Finogeev⁵⁶, F.M. Fionda²⁵, E.M. Fiore³³,
 M.G. Fleck⁹³, M. Floris³⁶, S. Foertsch⁶⁵, P. Foka⁹⁶, S. Fokin⁹⁹, E. Fragiaco¹⁰⁹, A. Francescon^{30,36},
 U. Frankenfeld⁹⁶, U. Fuchs³⁶, C. Furget⁷¹, A. Furs⁵⁶, M. Fusco Girard³¹, J.J. Gaardhøje⁸⁰, M. Gagliardi²⁷,
 A.M. Gago¹⁰², M. Gallio²⁷, D.R. Gangadharan⁷⁴, P. Ganoti^{36,88}, C. Gao⁷, C. Garabatos⁹⁶, E. Garcia-Solis¹³,
 C. Gargiulo³⁶, P. Gasik^{37,92}, E.F. Gauger¹¹⁸, M. Germain¹¹³, A. Gheata³⁶, M. Gheata^{62,36}, P. Ghosh¹³²,
 S.K. Ghosh⁴, P. Gianotti⁷², P. Giubellino^{36,110}, P. Giubileo³⁰, E. Gladysz-Dziadus¹¹⁷, P. Glässel⁹³,
 D.M. Gómez Coral⁶⁴, A. Gomez Ramirez⁵², V. Gonzalez¹⁰, P. González-Zamora¹⁰, S. Gorbunov⁴³,
 L. Görlich¹¹⁷, S. Gotovac¹¹⁶, V. Grabski⁶⁴, O.A. Grachov¹³⁶, L.K. Graczykowski¹³³, K.L. Graham¹⁰¹,
 A. Grelli⁵⁷, A. Grigoras³⁶, C. Grigoras³⁶, V. Grigoriev⁷⁵, A. Grigoryan¹, S. Grigoryan⁶⁶, B. Grinyov³,
 N. Grion¹⁰⁹, J.M. Gronefeld⁹⁶, J.F. Grosse-Oetringhaus³⁶, J.-Y. Grossiord¹³⁰, R. Grosso⁹⁶, F. Guber⁵⁶,
 R. Guernane⁷¹, B. Guerzoni²⁸, K. Gulbrandsen⁸⁰, T. Gunji¹²⁷, A. Gupta⁹⁰, R. Gupta⁹⁰, R. Haake⁵⁴,
 Ø. Haaland¹⁸, C. Hadjidakis⁵¹, M. Haiduc⁶², H. Hamagaki¹²⁷, G. Hamar¹³⁵, J.W. Harris¹³⁶, A. Harton¹³,
 D. Hatzifotiadou¹⁰⁴, S. Hayashi¹²⁷, S.T. Heckel⁵³, M. Heide⁵⁴, H. Helstrup³⁸, A. Hergelegiu⁷⁸, G. Herrera
 Corral¹¹, B.A. Hess³⁵, K.F. Hetland³⁸, H. Hillemanns³⁶, B. Hippolyte⁵⁵, R. Hosokawa¹²⁸, P. Hristov³⁶,
 M. Huang¹⁸, T.J. Humanic²⁰, N. Hussain⁴⁵, T. Hussain¹⁹, D. Hutter⁴³, D.S. Hwang²¹, R. Ilkaev⁹⁸,
 M. Inaba¹²⁸, M. Ippolitov^{75,99}, M. Irfan¹⁹, M. Ivanov⁹⁶, V. Ivanov⁸⁵, V. Izucheev¹¹¹, P.M. Jacobs⁷⁴,

M.B. Jadhav⁴⁸, S. Jadlovská¹¹⁵, J. Jadlovský^{115,59}, C. Jahnke¹²⁰, M.J. Jakubowska¹³³, H.J. Jang⁶⁸,
 M.A. Janik¹³³, P.H.S.Y. Jayarathna¹²², C. Jena³⁰, S. Jena¹²², R.T. Jimenez Bustamante⁹⁶, P.G. Jones¹⁰¹,
 H. Jung⁴⁴, A. Jusko¹⁰¹, P. Kalinak⁵⁹, A. Kalweit³⁶, J. Kamin⁵³, J.H. Kang¹³⁷, V. Kaplin⁷⁵, S. Kar¹³²,
 A. Karasu Uysal⁶⁹, O. Karavichev⁵⁶, T. Karavicheva⁵⁶, L. Karayan^{96,93}, E. Karpechev⁵⁶, U. Kebschull⁵²,
 R. Keidel¹³⁸, D.L.D. Keijdener⁵⁷, M. Keil³⁶, M. Mohisin Khan¹⁹, P. Khan¹⁰⁰, S.A. Khan¹³², A. Khanzadeev⁸⁵,
 Y. Kharlov¹¹¹, B. Kileng³⁸, D.W. Kim⁴⁴, D.J. Kim¹²³, D. Kim¹³⁷, H. Kim¹³⁷, J.S. Kim⁴⁴, M. Kim⁴⁴,
 M. Kim¹³⁷, S. Kim²¹, T. Kim¹³⁷, S. Kirsch⁴³, I. Kisel⁴³, S. Kiselev⁵⁸, A. Kisiel¹³³, G. Kiss¹³⁵, J.L. Klay⁶,
 C. Klein⁵³, J. Klein^{36,93}, C. Klein-Bösing⁵⁴, S. Klewin⁹³, A. Kluge³⁶, M.L. Knichel⁹³, A.G. Knospe¹¹⁸,
 T. Kobayashi¹²⁸, C. Kobdaj¹¹⁴, M. Kofarago³⁶, T. Kollegger^{96,43}, A. Kolojvari¹³¹, V. Kondratiev¹³¹,
 N. Kondratyeva⁷⁵, E. Kondratyuk¹¹¹, A. Konevskikh⁵⁶, M. Kopcik¹¹⁵, M. Kour⁹⁰, C. Kouzinopoulos³⁶,
 O. Kovalenko⁷⁷, V. Kovalenko¹³¹, M. Kowalski¹¹⁷, G. Koyithatta Meethalevedu⁴⁸, I. Králik⁵⁹,
 A. Kravčáková⁴¹, M. Kretz⁴³, M. Krivda^{59,101}, F. Krizek⁸³, E. Kryshen³⁶, M. Krzewicki⁴³, A.M. Kubera²⁰,
 V. Kučera⁸³, C. Kuhn⁵⁵, P.G. Kuijjer⁸¹, A. Kumar⁹⁰, J. Kumar⁴⁸, L. Kumar⁸⁷, S. Kumar⁴⁸, P. Kurashvili⁷⁷,
 A. Kurepin⁵⁶, A.B. Kurepin⁵⁶, A. Kuryakin⁹⁸, M.J. Kweon⁵⁰, Y. Kwon¹³⁷, S.L. La Pointe¹¹⁰, P. La Rocca²⁹,
 P. Ladron de Guevara¹¹, C. Lagana Fernandes¹²⁰, I. Lakomov³⁶, R. Langoy⁴², C. Lara⁵², A. Lardeux¹⁵,
 A. Lattuca²⁷, E. Laudi³⁶, R. Lea²⁶, L. Leardini⁹³, G.R. Lee¹⁰¹, S. Lee¹³⁷, F. Lehas⁸¹, R.C. Lemmon⁸²,
 V. Lenti¹⁰³, E. Leogrande⁵⁷, I. León Monzón¹¹⁹, H. León Vargas⁶⁴, M. Leonicino²⁷, P. Lévai¹³⁵, S. Li^{70,7},
 X. Li¹⁴, J. Lien⁴², R. Lietava¹⁰¹, S. Lindal²², V. Lindenstruth⁴³, C. Lippmann⁹⁶, M.A. Lisa²⁰,
 H.M. Ljunggren³⁴, D.F. Lodato⁵⁷, P.I. Loenne¹⁸, V. Loginov⁷⁵, C. Loizides⁷⁴, X. Lopez⁷⁰, E. López Torres⁹,
 A. Lowe¹³⁵, P. Luettig⁵³, M. Lunardon³⁰, G. Luparello²⁶, A. Maevskaya⁵⁶, M. Mager³⁶, S. Mahajan⁹⁰,
 S.M. Mahmood²², A. Maire⁵⁵, R.D. Majka¹³⁶, M. Malaev⁸⁵, I. Maldonado Cervantes⁶³, L. Malinina^{iii,66},
 D. Mal'Kevich⁵⁸, P. Malzacher⁹⁶, A. Mamonov⁹⁸, V. Manko⁹⁹, F. Manso⁷⁰, V. Manzari^{36,103},
 M. Marchisone^{27,65,126}, J. Mareš⁶⁰, G.V. Margagliotti²⁶, A. Margotti¹⁰⁴, J. Margutti⁵⁷, A. Marín⁹⁶,
 C. Markert¹¹⁸, M. Marquard⁵³, N.A. Martin⁹⁶, J. Martin Blanco¹¹³, P. Martinengo³⁶, M.I. Martínez²,
 G. Martínez García¹¹³, M. Martínez Pedreira³⁶, A. Mas¹²⁰, S. Masciocchi⁹⁶, M. Maserà²⁷, A. Masoni¹⁰⁵,
 L. Massacrier¹¹³, A. Mastroserio³³, A. Matyja¹¹⁷, C. Mayer¹¹⁷, J. Mazer¹²⁵, M.A. Mazzoni¹⁰⁸,
 D. McDonald¹²², F. Meddi²⁴, Y. Melikyan⁷⁵, A. Menchaca-Rocha⁶⁴, E. Meninno³¹, J. Mercado Pérez⁹³,
 M. Meres³⁹, Y. Miake¹²⁸, M.M. Mieskolainen⁴⁶, K. Mikhaylov^{66,58}, L. Milano³⁶, J. Milosevic²²,
 L.M. Minervini^{103,23}, A. Mischke⁵⁷, A.N. Mishra⁴⁹, D. Miśkowiec⁹⁶, J. Mitra¹³², C.M. Mitu⁶²,
 N. Mohammadi⁵⁷, B. Mohanty^{79,132}, L. Molnar^{55,113}, L. Montaño Zetina¹¹, E. Montes¹⁰, D.A. Moreira De
 Godoy^{54,113}, L.A.P. Moreno², S. Moretto³⁰, A. Morreale¹¹³, A. Morsch³⁶, V. Muccifora⁷², E. Mudnic¹¹⁶,
 D. Mühlheim⁵⁴, S. Muhuri¹³², M. Mukherjee¹³², J.D. Mulligan¹³⁶, M.G. Munhoz¹²⁰, R.H. Munzer^{92,37},
 S. Murray⁶⁵, L. Musa³⁶, J. Musinsky⁵⁹, B. Naik⁴⁸, R. Nair⁷⁷, B.K. Nandi⁴⁸, R. Nania¹⁰⁴, E. Nappi¹⁰³,
 M.U. Naru¹⁶, H. Natal da Luz¹²⁰, C. Nattrass¹²⁵, K. Nayak⁷⁹, T.K. Nayak¹³², S. Nazarenko⁹⁸, A. Nedosekin⁵⁸,
 L. Nellen⁶³, F. Ng¹²², M. Nicassio⁹⁶, M. Niculescu⁶², J. Niedziela³⁶, B.S. Nielsen⁸⁰, S. Nikolaev⁹⁹,
 S. Nikulin⁹⁹, V. Nikulin⁸⁵, F. Noferini^{12,104}, P. Nomokonov⁶⁶, G. Nooren⁵⁷, J.C.C. Noris², J. Norman¹²⁴,
 A. Nyman⁹⁹, J. Nystrand¹⁸, H. Oeschler⁹³, S. Oh¹³⁶, S.K. Oh⁶⁷, A. Ohlson³⁶, A. Okatan⁶⁹, T. Okubo⁴⁷,
 L. Olah¹³⁵, J. Oleniacz¹³³, A.C. Oliveira Da Silva¹²⁰, M.H. Oliver¹³⁶, J. Onderwaater⁹⁶, C. Oppedisano¹¹⁰,
 R. Orava⁴⁶, A. Ortiz Velasquez⁶³, A. Oskarsson³⁴, J. Otwinowski¹¹⁷, K. Oyama^{93,76}, M. Ozdemir⁵³,
 Y. Pachmayer⁹³, P. Pagano³¹, G. Paic⁶³, S.K. Pal¹³², J. Pan¹³⁴, A.K. Pandey⁴⁸, P. Papcun¹¹⁵, V. Papikyan¹,
 G.S. Pappalardo¹⁰⁶, P. Pareek⁴⁹, W.J. Park⁹⁶, S. Parmar⁸⁷, A. Passfeld⁵⁴, V. Patichio¹⁰³, R.N. Patra¹³²,
 B. Paul¹⁰⁰, T. Peitzmann⁵⁷, H. Pereira Da Costa¹⁵, E. Pereira De Oliveira Filho¹²⁰, D. Peresunko^{99,75},
 C.E. Pérez Lara⁸¹, E. Perez Lezama⁵³, V. Peskov⁵³, Y. Pestov⁵, V. Petráček⁴⁰, V. Petrov¹¹¹, M. Petrovici⁷⁸,
 C. Petta²⁹, S. Piano¹⁰⁹, M. Pikna³⁹, P. Pillot¹¹³, O. Pinazza^{104,36}, L. Pinsky¹²², D.B. Piyarathna¹²²,
 M. Płoskoń⁷⁴, M. Planinic¹²⁹, J. Pluta¹³³, S. Pochybova¹³⁵, P.L.M. Podesta-Lerma¹¹⁹, M.G. Poghosyan^{84,86},
 B. Polichtchouk¹¹¹, N. Poljak¹²⁹, W. Poonsawat¹¹⁴, A. Pop⁷⁸, S. Porteboeuf-Houssais⁷⁰, J. Porter⁷⁴,
 J. Pospisil⁸³, S.K. Prasad⁴, R. Preghenella^{36,104}, F. Prino¹¹⁰, C.A. Pruneau¹³⁴, I. Pshenichnov⁵⁶, M. Puccio²⁷,
 G. Puddu²⁵, P. Pujahari¹³⁴, V. Punin⁹⁸, J. Putschke¹³⁴, H. Qvigstad²², A. Rachevski¹⁰⁹, S. Raha⁴, S. Rajput⁹⁰,
 J. Rak¹²³, A. Rakotozafindrabe¹⁵, L. Ramello³², F. Rami⁵⁵, R. Raniwala⁹¹, S. Raniwala⁹¹, S.S. Räsänen⁴⁶,
 B.T. Rascanu⁵³, D. Rathee⁸⁷, K.F. Read^{125,84}, K. Redlich⁷⁷, R.J. Reed¹³⁴, A. Rehman¹⁸, P. Reichelt⁵³,
 F. Reidt^{93,36}, X. Ren⁷, R. Renfordt⁵³, A.R. Reolon⁷², A. Reshetin⁵⁶, J.-P. Revol¹², K. Reygers⁹³, V. Riabov⁸⁵,
 R.A. Ricci⁷³, T. Richert³⁴, M. Richter²², P. Riedler³⁶, W. Riegler³⁶, F. Riggi²⁹, C. Ristea⁶², E. Rocco⁵⁷,
 M. Rodríguez Cahuantzi^{2,11}, A. Rodríguez Manso⁸¹, K. Røed²², E. Rogochaya⁶⁶, D. Rohr⁴³, D. Röhrich¹⁸,
 R. Romita¹²⁴, F. Ronchetti^{72,36}, L. Ronflette¹¹³, P. Rosnet⁷⁰, A. Rossi^{30,36}, F. Roukoutakis⁸⁸, A. Roy⁴⁹,
 C. Roy⁵⁵, P. Roy¹⁰⁰, A.J. Rubio Montero¹⁰, R. Rui²⁶, R. Russo²⁷, E. Ryabinkin⁹⁹, Y. Ryabov⁸⁵,
 A. Rybicki¹¹⁷, S. Sadovsky¹¹¹, K. Šafařík³⁶, B. Sahlmüller⁵³, P. Sahoo⁴⁹, R. Sahoo⁴⁹, S. Sahoo⁶¹,

P.K. Sahu⁶¹, J. Saini¹³², S. Sakai⁷², M.A. Saleh¹³⁴, J. Salzwedel²⁰, S. Sambyal⁹⁰, V. Samsonov⁸⁵, L. Šándor⁵⁹,
 A. Sandoval⁶⁴, M. Sano¹²⁸, D. Sarkar¹³², E. Scapparone¹⁰⁴, F. Scarlassara³⁰, C. Schiaua⁷⁸, R. Schicker⁹³,
 C. Schmidt⁹⁶, H.R. Schmidt³⁵, S. Schuchmann⁵³, J. Schukraft³⁶, M. Schulc⁴⁰, T. Schuster¹³⁶, Y. Schutz^{36,113},
 K. Schwarz⁹⁶, K. Schweda⁹⁶, G. Scioli²⁸, E. Scomparin¹¹⁰, R. Scott¹²⁵, M. Šefčík⁴¹, J.E. Seger⁸⁶,
 Y. Sekiguchi¹²⁷, D. Sekihata⁴⁷, I. Selyuzhenkov⁹⁶, K. Senosi⁶⁵, S. Senyukov^{3,36}, E. Serradilla^{10,64},
 A. Sevcenco⁶², A. Shabanov⁵⁶, A. Shabetai¹¹³, O. Shadura³, R. Shahoyan³⁶, A. Shangaraev¹¹¹, A. Sharma⁹⁰,
 M. Sharma⁹⁰, M. Sharma⁹⁰, N. Sharma¹²⁵, K. Shigaki⁴⁷, K. Shtejer^{9,27}, Y. Sibiriyak⁹⁹, S. Siddhanta¹⁰⁵,
 K.M. Sielewicz³⁶, T. Siemiarczuk⁷⁷, D. Silvermyr^{84,34}, C. Silvestre⁷¹, G. Simatovic¹²⁹, G. Simonetti³⁶,
 R. Singaraju¹³², R. Singh⁷⁹, S. Singha^{132,79}, V. Singhal¹³², B.C. Sinha¹³², T. Sinha¹⁰⁰, B. Sitar³⁹, M. Sitta³²,
 T.B. Skaali²², M. Slupecki¹²³, N. Smirnov¹³⁶, R.J.M. Snellings⁵⁷, T.W. Snellman¹²³, C. Sogaard³⁴, J. Song⁹⁵,
 M. Song¹³⁷, Z. Song⁷, F. Soramel³⁰, S. Sorensen¹²⁵, F. Sozzi⁹⁶, M. Spacek⁴⁰, E. Spiriti⁷², I. Sputowska¹¹⁷,
 M. Spyropoulou-Stassinaki⁸⁸, J. Stachel⁹³, I. Stan⁶², G. Stefanek⁷⁷, E. Stenlund³⁴, G. Steyn⁶⁵, J.H. Stiller⁹³,
 D. Stocco¹¹³, P. Strmen³⁹, A.A.P. Suaide¹²⁰, T. Sugitate⁴⁷, C. Suire⁵¹, M. Suleymanov¹⁶, M. Suljic^{26,i},
 R. Sultanov⁵⁸, M. Šumbera⁸³, A. Szabo³⁹, A. Szanto de Toledo^{120,i}, I. Szarka³⁹, A. Szczepankiewicz³⁶,
 M. Szymanski¹³³, U. Tabassam¹⁶, J. Takahashi¹²¹, G.J. Tambave¹⁸, N. Tanaka¹²⁸, M.A. Tangaro³³,
 M. Tarhini⁵¹, M. Tariq¹⁹, M.G. Tarzila⁷⁸, A. Tauro³⁶, G. Tejada Muñoz², A. Telesca³⁶, K. Terasaki¹²⁷,
 C. Terrevoli³⁰, B. Teyssier¹³⁰, J. Thäder⁷⁴, D. Thomas¹¹⁸, R. Tieulent¹³⁰, A.R. Timmins¹²², A. Toia⁵³,
 S. Trogolo²⁷, G. Trombetta³³, V. Trubnikov³, W.H. Trzaska¹²³, T. Tsuji¹²⁷, A. Tumkin⁹⁸, R. Turrisi¹⁰⁷,
 T.S. Tveter²², K. Ullaland¹⁸, A. Uras¹³⁰, G.L. Usai²⁵, A. Utrobicic¹²⁹, M. Vajzer⁸³, M. Vala⁵⁹, L. Valencia
 Palomo⁷⁰, S. Vallero²⁷, J. Van Der Maarel⁵⁷, J.W. Van Hoorne³⁶, M. van Leeuwen⁵⁷, T. Vanat⁸³, P. Vande
 Vyvre³⁶, D. Varga¹³⁵, A. Vargas², M. Vargyas¹²³, R. Varma⁴⁸, M. Vasileiou⁸⁸, A. Vasiliev⁹⁹, A. Vauthier⁷¹,
 V. Vechemin¹³¹, A.M. Veen⁵⁷, M. Veldhoen⁵⁷, A. Velure¹⁸, M. Venaruzzo⁷³, E. Vercellin²⁷, S. Vergara
 Limón², R. Vernet⁸, M. Verweij¹³⁴, L. Vickovic¹¹⁶, G. Viesti^{30,i}, J. Viinikainen¹²³, Z. Vilakazi¹²⁶,
 O. Villalobos Baillie¹⁰¹, A. Villatoro Tello², A. Vinogradov⁹⁹, L. Vinogradov¹³¹, Y. Vinogradov^{98,i},
 T. Virgili³¹, V. Vislavicius³⁴, Y.P. Viyogi¹³², A. Vodopyanov⁶⁶, M.A. Völkl⁹³, K. Voloshin⁵⁸,
 S.A. Voloshin¹³⁴, G. Volpe¹³⁵, B. von Haller³⁶, I. Vorobyev^{37,92}, D. Vranic^{96,36}, J. Vrláková⁴¹,
 B. Vulpescu⁷⁰, A. Vyushin⁹⁸, B. Wagner¹⁸, J. Wagner⁹⁶, H. Wang⁵⁷, M. Wang^{7,113}, D. Watanabe¹²⁸,
 Y. Watanabe¹²⁷, M. Weber^{112,36}, S.G. Weber⁹⁶, D.F. Weiser⁹³, J.P. Wessels⁵⁴, U. Westerhoff⁵⁴,
 A.M. Whitehead⁸⁹, J. Wiechula³⁵, J. Wikne²², M. Wilde⁵⁴, G. Wilk⁷⁷, J. Wilkinson⁹³, M.C.S. Williams¹⁰⁴,
 B. Windelband⁹³, M. Winn⁹³, C.G. Yaldo¹³⁴, H. Yang⁵⁷, P. Yang⁷, S. Yano⁴⁷, C. Yasar⁶⁹, Z. Yin⁷,
 H. Yokoyama¹²⁸, I.-K. Yoo⁹⁵, J.H. Yoon⁵⁰, V. Yurchenko³, I. Yushmanov⁹⁹, A. Zaborowska¹³³, V. Zaccolo⁸⁰,
 A. Zaman¹⁶, C. Zampolli¹⁰⁴, H.J.C. Zanolli¹²⁰, S. Zaporozhets⁶⁶, N. Zardoshti¹⁰¹, A. Zarochentsev¹³¹,
 P. Závada⁶⁰, N. Zaviyalov⁹⁸, H. Zbroszczyk¹³³, I.S. Zgura⁶², M. Zhalov⁸⁵, H. Zhang¹⁸, X. Zhang⁷⁴,
 Y. Zhang⁷, C. Zhang⁵⁷, Z. Zhang⁷, C. Zhao²², N. Zhigareva⁵⁸, D. Zhou⁷, Y. Zhou⁸⁰, Z. Zhou¹⁸, H. Zhu¹⁸,
 J. Zhu^{113,7}, A. Zichichi^{28,12}, A. Zimmermann⁹³, M.B. Zimmermann^{54,36}, G. Zinovjev³, M. Zyzak⁴³

Affiliation notes

ⁱ Deceased

ⁱⁱ Also at: Georgia State University, Atlanta, Georgia, United States

ⁱⁱⁱ Also at: M.V. Lomonosov Moscow State University, D.V. Skobeltsyn Institute of Nuclear, Physics,
 Moscow, Russia

Collaboration Institutes

- ¹ A.I. Alikhanyan National Science Laboratory (Yerevan Physics Institute) Foundation, Yerevan, Armenia
- ² Benemérita Universidad Autónoma de Puebla, Puebla, Mexico
- ³ Bogolyubov Institute for Theoretical Physics, Kiev, Ukraine
- ⁴ Bose Institute, Department of Physics and Centre for Astroparticle Physics and Space Science (CAPSS),
 Kolkata, India
- ⁵ Budker Institute for Nuclear Physics, Novosibirsk, Russia
- ⁶ California Polytechnic State University, San Luis Obispo, California, United States
- ⁷ Central China Normal University, Wuhan, China
- ⁸ Centre de Calcul de l'IN2P3, Villeurbanne, France
- ⁹ Centro de Aplicaciones Tecnológicas y Desarrollo Nuclear (CEADEN), Havana, Cuba
- ¹⁰ Centro de Investigaciones Energéticas Medioambientales y Tecnológicas (CIEMAT), Madrid, Spain
- ¹¹ Centro de Investigación y de Estudios Avanzados (CINVESTAV), Mexico City and Mérida, Mexico

- 12 Centro Fermi - Museo Storico della Fisica e Centro Studi e Ricerche “Enrico Fermi”, Rome, Italy
- 13 Chicago State University, Chicago, Illinois, USA
- 14 China Institute of Atomic Energy, Beijing, China
- 15 Commissariat à l’Energie Atomique, IRFU, Saclay, France
- 16 COMSATS Institute of Information Technology (CIIT), Islamabad, Pakistan
- 17 Departamento de Física de Partículas and IGFAE, Universidad de Santiago de Compostela, Santiago de Compostela, Spain
- 18 Department of Physics and Technology, University of Bergen, Bergen, Norway
- 19 Department of Physics, Aligarh Muslim University, Aligarh, India
- 20 Department of Physics, Ohio State University, Columbus, Ohio, United States
- 21 Department of Physics, Sejong University, Seoul, South Korea
- 22 Department of Physics, University of Oslo, Oslo, Norway
- 23 Dipartimento di Elettrotecnica ed Elettronica del Politecnico, Bari, Italy
- 24 Dipartimento di Fisica dell’Università ‘La Sapienza’ and Sezione INFN Rome, Italy
- 25 Dipartimento di Fisica dell’Università and Sezione INFN, Cagliari, Italy
- 26 Dipartimento di Fisica dell’Università and Sezione INFN, Trieste, Italy
- 27 Dipartimento di Fisica dell’Università and Sezione INFN, Turin, Italy
- 28 Dipartimento di Fisica e Astronomia dell’Università and Sezione INFN, Bologna, Italy
- 29 Dipartimento di Fisica e Astronomia dell’Università and Sezione INFN, Catania, Italy
- 30 Dipartimento di Fisica e Astronomia dell’Università and Sezione INFN, Padova, Italy
- 31 Dipartimento di Fisica ‘E.R. Caianiello’ dell’Università and Gruppo Collegato INFN, Salerno, Italy
- 32 Dipartimento di Scienze e Innovazione Tecnologica dell’Università del Piemonte Orientale and Gruppo Collegato INFN, Alessandria, Italy
- 33 Dipartimento Interateneo di Fisica ‘M. Merlin’ and Sezione INFN, Bari, Italy
- 34 Division of Experimental High Energy Physics, University of Lund, Lund, Sweden
- 35 Eberhard Karls Universität Tübingen, Tübingen, Germany
- 36 European Organization for Nuclear Research (CERN), Geneva, Switzerland
- 37 Excellence Cluster Universe, Technische Universität München, Munich, Germany
- 38 Faculty of Engineering, Bergen University College, Bergen, Norway
- 39 Faculty of Mathematics, Physics and Informatics, Comenius University, Bratislava, Slovakia
- 40 Faculty of Nuclear Sciences and Physical Engineering, Czech Technical University in Prague, Prague, Czech Republic
- 41 Faculty of Science, P.J. Šafárik University, Košice, Slovakia
- 42 Faculty of Technology, Buskerud and Vestfold University College, Vestfold, Norway
- 43 Frankfurt Institute for Advanced Studies, Johann Wolfgang Goethe-Universität Frankfurt, Frankfurt, Germany
- 44 Gangneung-Wonju National University, Gangneung, South Korea
- 45 Gauhati University, Department of Physics, Guwahati, India
- 46 Helsinki Institute of Physics (HIP), Helsinki, Finland
- 47 Hiroshima University, Hiroshima, Japan
- 48 Indian Institute of Technology Bombay (IIT), Mumbai, India
- 49 Indian Institute of Technology Indore, Indore (IITI), India
- 50 Inha University, Incheon, South Korea
- 51 Institut de Physique Nucléaire d’Orsay (IPNO), Université Paris-Sud, CNRS-IN2P3, Orsay, France
- 52 Institut für Informatik, Johann Wolfgang Goethe-Universität Frankfurt, Frankfurt, Germany
- 53 Institut für Kernphysik, Johann Wolfgang Goethe-Universität Frankfurt, Frankfurt, Germany
- 54 Institut für Kernphysik, Westfälische Wilhelms-Universität Münster, Münster, Germany
- 55 Institut Pluridisciplinaire Hubert Curien (IPHC), Université de Strasbourg, CNRS-IN2P3, Strasbourg, France
- 56 Institute for Nuclear Research, Academy of Sciences, Moscow, Russia
- 57 Institute for Subatomic Physics of Utrecht University, Utrecht, Netherlands
- 58 Institute for Theoretical and Experimental Physics, Moscow, Russia
- 59 Institute of Experimental Physics, Slovak Academy of Sciences, Košice, Slovakia
- 60 Institute of Physics, Academy of Sciences of the Czech Republic, Prague, Czech Republic
- 61 Institute of Physics, Bhubaneswar, India
- 62 Institute of Space Science (ISS), Bucharest, Romania

- 63 Instituto de Ciencias Nucleares, Universidad Nacional Autónoma de México, Mexico City, Mexico
 64 Instituto de Física, Universidad Nacional Autónoma de México, Mexico City, Mexico
 65 iThemba LABS, National Research Foundation, Somerset West, South Africa
 66 Joint Institute for Nuclear Research (JINR), Dubna, Russia
 67 Konkuk University, Seoul, South Korea
 68 Korea Institute of Science and Technology Information, Daejeon, South Korea
 69 KTO Karatay University, Konya, Turkey
 70 Laboratoire de Physique Corpusculaire (LPC), Clermont Université, Université Blaise Pascal, CNRS–IN2P3, Clermont-Ferrand, France
 71 Laboratoire de Physique Subatomique et de Cosmologie, Université Grenoble-Alpes, CNRS-IN2P3, Grenoble, France
 72 Laboratori Nazionali di Frascati, INFN, Frascati, Italy
 73 Laboratori Nazionali di Legnaro, INFN, Legnaro, Italy
 74 Lawrence Berkeley National Laboratory, Berkeley, California, United States
 75 Moscow Engineering Physics Institute, Moscow, Russia
 76 Nagasaki Institute of Applied Science, Nagasaki, Japan
 77 National Centre for Nuclear Studies, Warsaw, Poland
 78 National Institute for Physics and Nuclear Engineering, Bucharest, Romania
 79 National Institute of Science Education and Research, Bhubaneswar, India
 80 Niels Bohr Institute, University of Copenhagen, Copenhagen, Denmark
 81 Nikhef, Nationaal instituut voor subatomaire fysica, Amsterdam, Netherlands
 82 Nuclear Physics Group, STFC Daresbury Laboratory, Daresbury, United Kingdom
 83 Nuclear Physics Institute, Academy of Sciences of the Czech Republic, Řež u Prahy, Czech Republic
 84 Oak Ridge National Laboratory, Oak Ridge, Tennessee, United States
 85 Petersburg Nuclear Physics Institute, Gatchina, Russia
 86 Physics Department, Creighton University, Omaha, Nebraska, United States
 87 Physics Department, Panjab University, Chandigarh, India
 88 Physics Department, University of Athens, Athens, Greece
 89 Physics Department, University of Cape Town, Cape Town, South Africa
 90 Physics Department, University of Jammu, Jammu, India
 91 Physics Department, University of Rajasthan, Jaipur, India
 92 Physik Department, Technische Universität München, Munich, Germany
 93 Physikalisches Institut, Ruprecht-Karls-Universität Heidelberg, Heidelberg, Germany
 94 Purdue University, West Lafayette, Indiana, United States
 95 Pusan National University, Pusan, South Korea
 96 Research Division and ExtreMe Matter Institute EMMI, GSI Helmholtzzentrum für Schwerionenforschung, Darmstadt, Germany
 97 Rudjer Bošković Institute, Zagreb, Croatia
 98 Russian Federal Nuclear Center (VNIIEF), Sarov, Russia
 99 Russian Research Centre Kurchatov Institute, Moscow, Russia
 100 Saha Institute of Nuclear Physics, Kolkata, India
 101 School of Physics and Astronomy, University of Birmingham, Birmingham, United Kingdom
 102 Sección Física, Departamento de Ciencias, Pontificia Universidad Católica del Perú, Lima, Peru
 103 Sezione INFN, Bari, Italy
 104 Sezione INFN, Bologna, Italy
 105 Sezione INFN, Cagliari, Italy
 106 Sezione INFN, Catania, Italy
 107 Sezione INFN, Padova, Italy
 108 Sezione INFN, Rome, Italy
 109 Sezione INFN, Trieste, Italy
 110 Sezione INFN, Turin, Italy
 111 SSC IHEP of NRC Kurchatov institute, Protvino, Russia
 112 Stefan Meyer Institut für Subatomare Physik (SMI), Vienna, Austria
 113 SUBATECH, Ecole des Mines de Nantes, Université de Nantes, CNRS-IN2P3, Nantes, France
 114 Suranaree University of Technology, Nakhon Ratchasima, Thailand
 115 Technical University of Košice, Košice, Slovakia

- 116 Technical University of Split FESB, Split, Croatia
- 117 The Henryk Niewodniczanski Institute of Nuclear Physics, Polish Academy of Sciences, Cracow, Poland
- 118 The University of Texas at Austin, Physics Department, Austin, Texas, USA
- 119 Universidad Autónoma de Sinaloa, Culiacán, Mexico
- 120 Universidade de São Paulo (USP), São Paulo, Brazil
- 121 Universidade Estadual de Campinas (UNICAMP), Campinas, Brazil
- 122 University of Houston, Houston, Texas, United States
- 123 University of Jyväskylä, Jyväskylä, Finland
- 124 University of Liverpool, Liverpool, United Kingdom
- 125 University of Tennessee, Knoxville, Tennessee, United States
- 126 University of the Witwatersrand, Johannesburg, South Africa
- 127 University of Tokyo, Tokyo, Japan
- 128 University of Tsukuba, Tsukuba, Japan
- 129 University of Zagreb, Zagreb, Croatia
- 130 Université de Lyon, Université Lyon 1, CNRS/IN2P3, IPN-Lyon, Villeurbanne, France
- 131 V. Fock Institute for Physics, St. Petersburg State University, St. Petersburg, Russia
- 132 Variable Energy Cyclotron Centre, Kolkata, India
- 133 Warsaw University of Technology, Warsaw, Poland
- 134 Wayne State University, Detroit, Michigan, United States
- 135 Wigner Research Centre for Physics, Hungarian Academy of Sciences, Budapest, Hungary
- 136 Yale University, New Haven, Connecticut, United States
- 137 Yonsei University, Seoul, South Korea
- 138 Zentrum für Technologietransfer und Telekommunikation (ZTT), Fachhochschule Worms, Worms, Germany